Contents

4 Photon Beam **2**

4.1 Choice of technique . . . 3
4.1.1 Compton back-scatter . . . 4
4.1.2 Tagged bremsstrahlung . . . 6
4.1.3 Coherent bremsstrahlung . . . 7
4.2 Photon Source . . . 9
4.2.1 Essential features . . . 11
4.2.2 Use of collimation . . . 12
4.2.3 Choice of radiator . . . 20
4.2.4 Crystal thickness . . . 23
4.2.5 Crystal mount . . . 26
4.2.6 Crystal alignment and monitoring . . . 28
4.2.7 Crystal quality and lifetime . . . 28
4.3 Electron Beam . . . 32
4.3.1 Beam polarization . . . 32
4.3.2 Beam emittance . . . 34
4.3.3 Electron beam line optics . . . 36
4.3.4 Electron beam dump . . . 40
4.3.5 Beam containment and shielding . . . 41
4.4 Tagging Spectrometer . . . 42
4.4.1 Specifications . . . 42
4.4.2 Magnet . . . 42
4.4.3 Spectrometer optics . . . 45
4.4.4 Tagger detectors . . . 47
4.4.5 Beam dump optics . . . 48
4.5 Polarimetry Instrumentation . . . 48
4.6 Operating Beam Intensity . . . 50

Chapter 4

Photon Beam

One of the unique opportunities presented by a CEBAF upgrade to energies of 12 GeV and beyond is the possibility of generating high-intensity c.w. photon beams for high-energy photoproduction experiments. In this regime, photon beams represent an interesting extension to the meson spectroscopy program that has been actively pursued using beams of pseudoscalar mesons at hadron accelerator laboratories: with high energy photons one has essentially a beam of *vector* mesons. It is difficult, in fact, to conceive of any other way to obtain such a vector beam.

The requirements for photon beam energy and polarization were described in chapter 3. This chapter describes a design for a real photon facility that meets these requirements. Starting with a beam of monochromatic electrons, it provides an intense beam of high-energy photons with an energy spectrum that is dominated by a single peak. A significant fraction of the total power in the beam is concentrated inside this peak, which has a width of less than 10% f.w.h.m. At a fixed electron beam energy E_0, the peak energy of the photon beam can be varied anywhere up to 90% E_0 simply by rotating a crystal. The photon spectrum inside the intensity peak has a large degree of linear polarization. The precise energy of an individual photon inside the peak is determined ("tagged") from the momentum of the recoil electron measured in a dedicated "tagging" spectrometer. The design is formed around the expected parameters for the CEBAF beam following the energy upgrade to 12 GeV, although nothing prevents its operation at lower energies before the time that 12 GeV beams are available.

This chapter begins with a survey of the techniques for producing high-energy photons that were considered in the development of this design, and the reasons for the choice of coherent bremsstrahlung. The coherent bremsstrahlung source is then described in greater detail, followed by a discussion

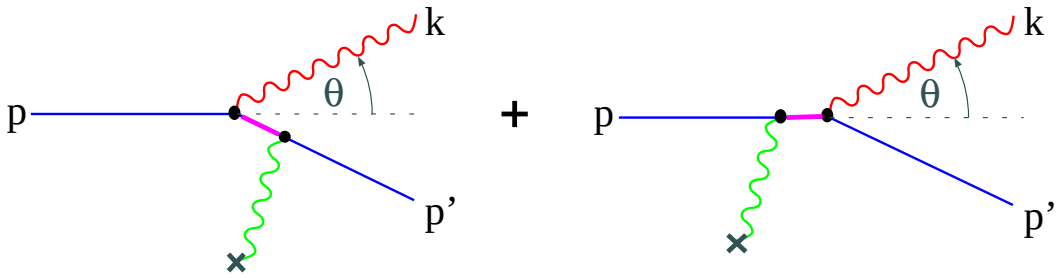

Figure 4.1: Generic diagrams for hard photon production from a high energy electron beam. The symbol × represents either a static charge distribution, in the case of virtual photons in the initial state (i.e. bremsstrahlung), or an optical cavity, in the case of real photons in the initial state (i.e. Compton scattering).

of the requirements that the design places on the electron beam that feeds the source. The tagging spectrometer design is described next, and the chapter concludes with a discussion of the considerations that govern the choice of beam intensity for particular measurements.

4.1 Choice of technique

Two basic methods have been considered for producing photons of the highest possible energy, flux and polarization from electrons of 12 GeV. The methods are bremsstrahlung and Compton scattering of light. Both are well-established methods of producing photon beams. Both techniques are actually described by the same Feynman diagrams, shown in Fig. 4.1. In the case of Compton scattering the incoming photon is real, whereas it is virtual for the case of bremsstrahlung.

Each of these techniques has its own limitations and advantages. In order to be suitable for HALL D, the photon source must be capable of producing photons of energy at least 80% E_0. The photon beam should have linear polarization. The energy resolution for individual photons in the beam should be as good as possible, *i.e.* on the order of the energy spread of the electron beam itself. It should be capable of producing fluxes up to 10^8/s. The contamination of the beam with photons outside the desired energy band should be as low as possible. It is also important that the source should be reliable and require a minimum of down-time for maintenance. The suitability of each approach is discussed below in the light of these criteria.

4.1.1 Compton back-scatter

A Compton source begins with a beam of visible or ultraviolet light, typically from a laser, that is aligned to intersect the incident electron beam at close to 180°. Some of the photons undergo Compton scattering with the beam electrons. In the lab frame, the scattered photons come out in a narrow cone about the incident electron direction, and carry a significant fraction of the electron energy.

The basic design of the Compton back-scatter source for this study was put forward by C. Keppel and R. Ent [1]. The design entails the use of a four-mirror high-gain cavity pumped by a 10kW argon-ion laser putting out $2\,ps$ pulses at a frequency of 100 MHz. The pulses in the cavity are synchronized so that the light pulses intercept an electron bucket each time they pass through the beam. The total length of the cavity is $2\,m$ with a crossing angle of 1°. Both cavity and electron beam are focused to a tiny spot of 10 μm r.m.s. radius at the crossing point. A small spot size is necessary in order to get as high a scattering rate as possible. The gain of the cavity is 10^4, which is conservative in view of recent advances in mirror technology. The wavelength of the light is $514\,nm$. The rate spectrum of the back-scattered beam from this source is shown in Fig 4.2a for a 1μA electron beam at 12 GeV.

From the point of view of flux, this source is marginal. With a few μA of beam and mirror improvements, it might produce 10^8 photons/s in the upper 1/3 of its energy spectrum. However, its maximum photon energy of 3.7 GeV is far short of the 80% E_0 needed for HALL D. To remedy this one must decrease the wavelength of the laser beam. This can be done by the use of a frequency-doubling crystal that absorbs the green light from the laser and produces ultraviolet light at $257\,nm$. Storing this light in a cavity of similar design to that described above yields the back-scatter rate spectrum shown in Fig. 4.2b. The major reason for the drop in rate is the decrease in the cavity gain from 10000 to 250. This is imposed by the diminished reflectivities of mirrors in the UV. Other factors are the inefficiency of the doubling crystal, a factor of two in rate from the doubling itself, and the decreasing Compton cross section with energy. The maximum photon energy is still under 50% E_0 and the flux is three orders of magnitude below the desired rate.

In order to reach photon energies of 80% E_0, initial photons of $20eV$ are needed. The brightest sources of these would be a synchrotron light source or a free electron laser (FEL). Mirrors that operate at these wavelengths typically have reflectivities around 70%. With these one could conceive of a scheme that uses a wiggler to extract energy from the 12 GeV beam before it enters the dump. This light would have the same time structure as incident beam, and

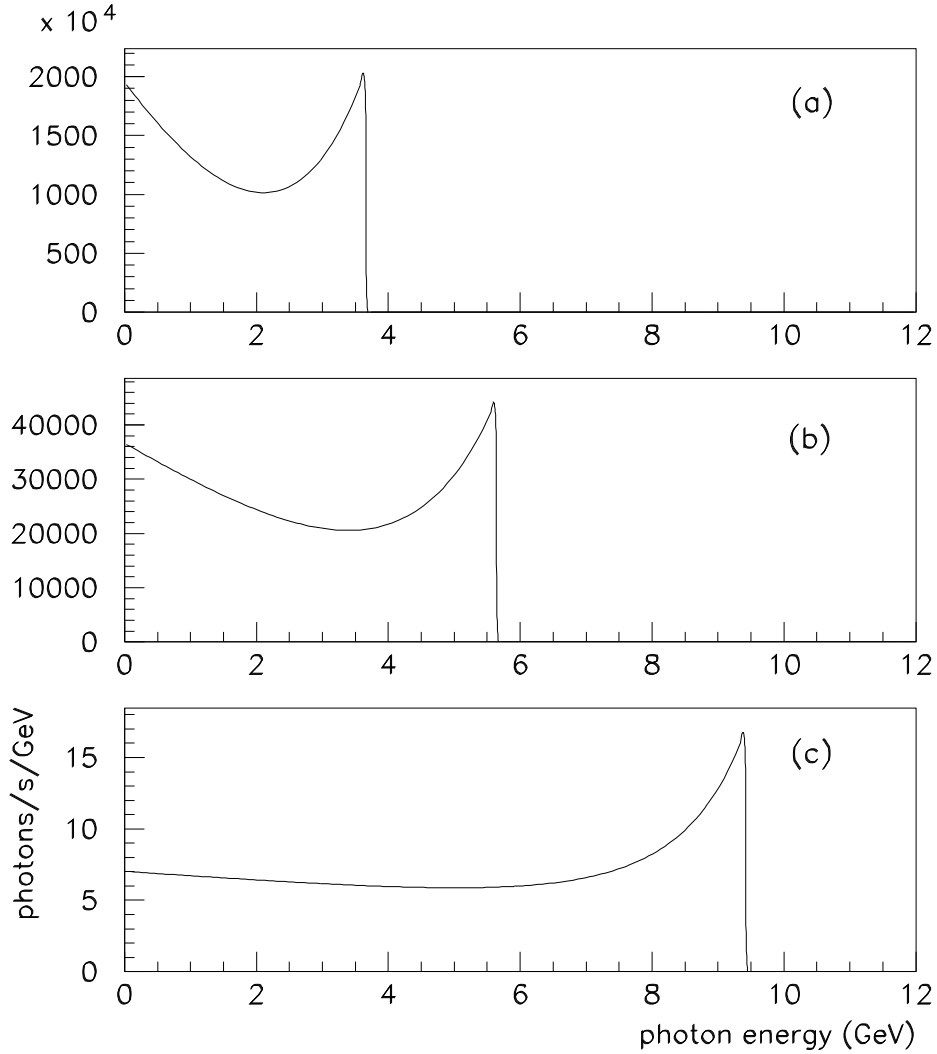

Figure 4.2: Photon energy spectrum from the Compton back-scatter source described in the text and a 12 GeV electron beam at 1μA. (a) cavity of gain 10000 driven by a 10kW Argon-ion laser (514 nm) pulsed at 100 MHz. (b) cavity of gain 250 driven by 3kW frequency-doubler (257nm) pulsed at 100 MHz. (c) cavity of gain 1 driven by a hypothetical FEL source operating at 20eV with the same time structure as CEBAF beam, peak power 1kW.

so it could be reflected back and made to cross the incident beam at a small angle, for a Compton back-scatter source. An indication of the level of flux that could be achieved with such a source can be obtained by using the laser cavity model described above, setting the gain to 1, the wavelength to 62 nm, and assuming 1kW peak (1W average) of synchrotron light. The back-scatter rate is shown in Fig 4.2c. This plot shows that even if the full power of a 1μA 12 GeV beam were converted into 20eV photons and backscattered from the incoming beam, the rate would still fall far short of the requirements for HALL D.

From the point of view of polarization, the Compton back-scatter source would be ideal. The polarization of the back-scattered beam is controlled by that of the laser, and can be essentially 100%. This source is also virtually background-free because the spectrum below any desired cutoff can be eliminated by collimation. The energy of the remaining beam can be measured to within the resolution of the electron beam by tagging. However the the combination of sufficient energy and sufficient flux for the purposes of HALL D cannot be achieved using this source.

4.1.2 Tagged bremsstrahlung

A bremsstrahlung source consists of a thin piece of material (the radiator) that is placed in the electron beam and converts part of the energy of the beam into bremsstrahlung radiation. Bremsstrahlung offers the only practical way, starting with an electron beam at CEBAF energies, to produce a photon beam with a significant flux in the vicinity of the end point. It produces a naturally collimated photon beam with a characteristic angular spread of m/E_0. This allows the low emittance of the CEBAF beam to be effectively transfered into the secondary photon beam.

Bremsstrahlung does not suffer from the kind of flux limitations that were encountered in the examination of Compton back-scatter sources. The radiator thickness must be kept below 1% of a radiation length in order to maintain good energy resolution in the tagger. Keeping the thickness below 10^{-3} radiation lengths ensures that multiple scattering in the radiator does not significantly broaden the divergence angle of the photon beam. A 10^{-3} radiator and 1μA of electrons would produce much more than sufficient flux for HALL D.

A bremsstrahlung source is, however, deficient in some other respects. Averaged over the bremsstrahlung cone, the photon beam has zero linear polarization. Circular polarization can be achieved by polarization transfer from a circularly polarized electron beam, but for the purposes of HALL D it is linear

polarization that is desired. A bremsstrahlung source also suffers from a large low-energy flux in the beam. The power spectrum of a bremsstrahlung beam is approximately uniform from zero up to the energy of the incident electrons. This means that an experiment that uses the high-energy part of the beam must operate in a background of low-energy photons that are many times more frequent. The tagger is helpful in eliminating many of the false starts in the detector that arise from the background, but this technique becomes ineffective at rates above a few 10^7 tagged photons/s. For the typical experiment using tagged bremsstrahlung and open detector geometry, background from low-energy beam particles limits the rate at which the experiment can run to less than $5 \cdot 10^7$ tagged photons/s. The goal for HALL D pushes that limit to 10^8/s by employing tagged *coherent* bremsstrahlung.

4.1.3 Coherent bremsstrahlung

The source described in the previous section meets most of the requirements for HALL D, but is deficient in the areas of polarization and backgrounds. Both of these deficiencies can be remedied by replacing the conventional amorphous or polycrystalline radiator with a thin mono-crystalline wafer. At special settings for the orientation of the crystal, the atoms in the radiator can be made to recoil together from the radiating electron. When they do this they produce a coherent enhancement at particular energies in the radiation spectrum, which correspond to the reciprocal lattice vectors of the crystal. The kinematics are such that a randomly oriented lattice vector would make a tiny peak located up at the end point of the energy spectrum, where the coherent gain factor is negligible. By careful orientation of the crystal, however, one of the lattice vectors can be aligned with the favored kinematics for bremsstrahlung, at which point its coherent peak appears well below the end point, and its coherent gain can be large enough that it contributes a large fraction of the total radiated power.

This is illustrated in Fig. 4.3. This plot shows the intensity ($E\ dN/dE$) or power spectrum of the coherent bremsstrahlung beam after collimation. The sequence of secondary peaks above the primary correspond to integral multiples of the primary reciprocal lattice vector and so they are always present. By careful choice of orientation angles it is possible to suppress all other vectors and isolate just one primary peak. By rotating the crystal, the position of the peak can be moved from one end of the spectrum to the other. Note that the coherent peaks appear on top of the incoherent bremsstrahlung continuum.

Unlike the underlying continuum, the photons in the coherent peak have significant net linear polarization in the plane given by the beam direction

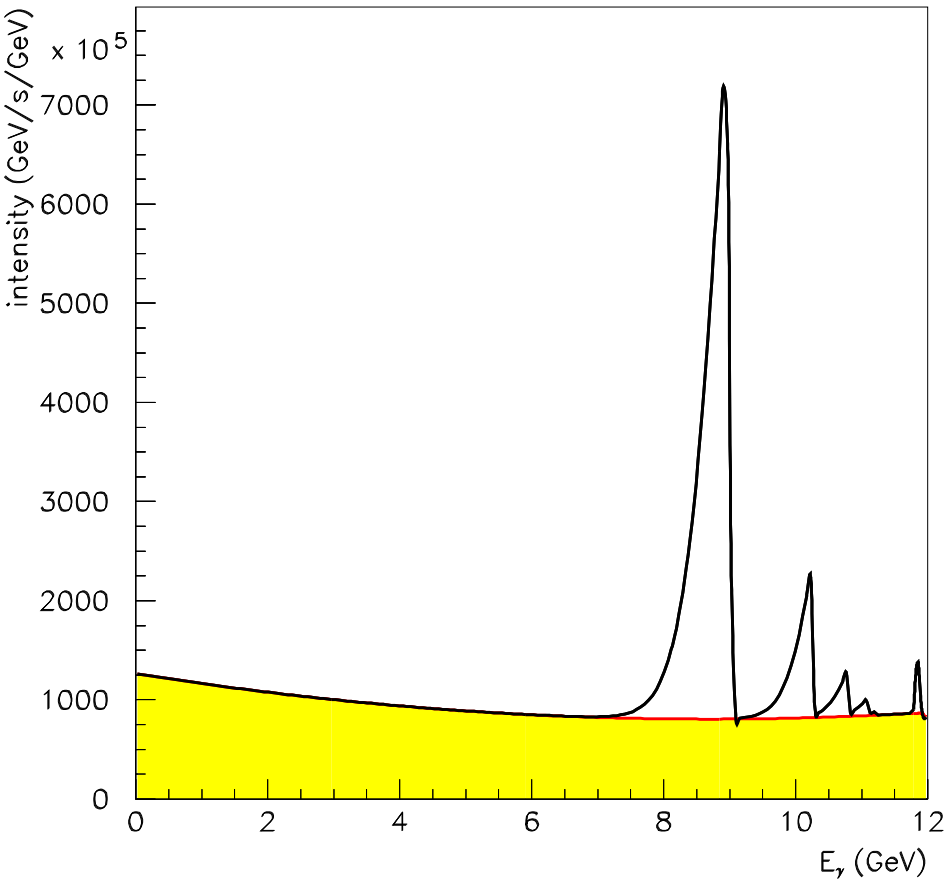

Figure 4.3: Photon power spectrum from an oriented diamond radiator. The y axis is dP/dE with power P expressed in GeV/s and E in GeV. The radiator thickness is 10^{-4} radiation lengths and the electron beam current is 1μA. Shown is what emerges after the photon beam passes through a collimator 3.4 mm in diameter located 80 m downstream from the radiator.

and the crystal lattice vector. This polarization is enhanced by collimating the photon beam beyond its intrinsic angular spread, as discussed in the next section. The loss in flux from collimation can be recovered by increasing the electron beam current. As will be shown in the following section, even in the case of very thin crystals and severe collimation, only modest electron beam currents are needed to produce the required photon flux.

The use of coherent bremsstrahlung improves the background conditions by increasing the ratio of hard to soft photons in the beam. For measurements that do not require polarization, a crystal radiator can be used without collimation to reduce the amount of low-energy background for a given rate of tagged photons. Where polarization is required, coherent bremsstrahlung is indispensable.

4.2 Photon Source

A horizontal plan view of the photon beam line is shown in Fig. 4.4 with the major components labelled. The electron beam enters the figure from below ground at the left and is bent into the horizontal plane to enter the tagger building. There it passes through two small dipoles to impinge upon the bremsstrahlung radiator. After its exit from the radiator, the electron beam passes into the tagging spectrometer where the primary beam is bent in the direction of the electron beam dump. The radiator crystal is thin enough that the average energy loss by the electrons in traversing the radiator is less than the intrinsic energy spread of the incident beam. Those electrons which lose a significant fraction of their initial energy inside the radiator do so by emitting a single bremsstrahlung photon. These degraded electrons are bent out of the primary beam inside the tagger magnet and exit the vacuum through a thin window, passing through air for a short distance to strike the focal plane of the spectrometer. The primary electron beam is contained inside vacuum all the way to the dump.

The photons that are produced in the radiator pass through a small hole bored in the return yoke of the tagger magnet in the forward direction. They then pass into an evacuated photon beam pipe and travel to the experimental hall. Just before entering the hall the photon beam passes through a system of collimators and sweeping magnets. In the figure they are shown in a separate enclosure for shielding purposes. The primary collimator is first. It defines the part of the photon beam that is allowed to reach the target. Debris from interactions along the inside surface of the collimator bore forms a halo around the photon beam that exits the primary collimator. The charged component of

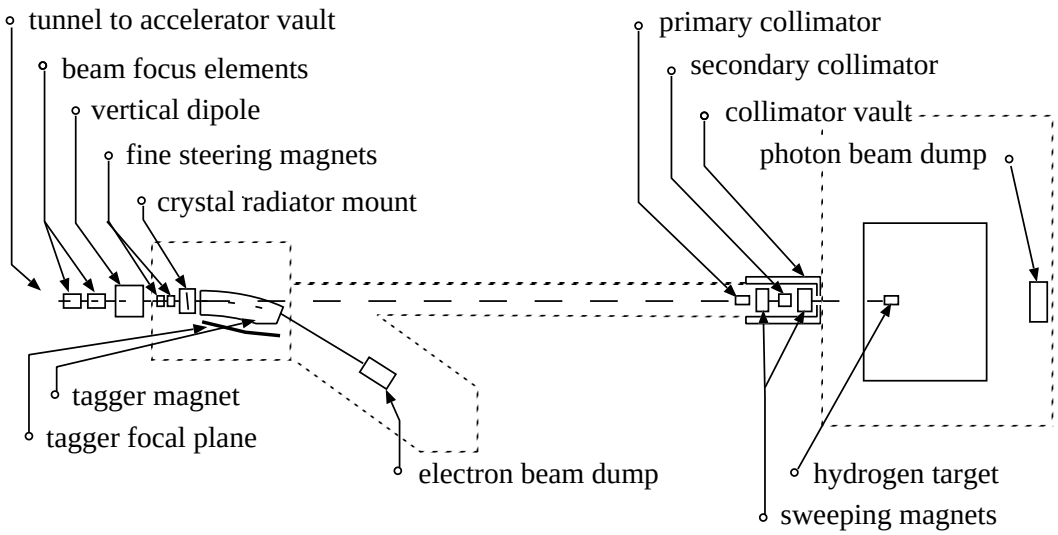

Figure 4.4: Schematic plan view of the photon beam line, shown in the horizontal plane as viewed from above. The objects in this figure are not drawn to scale.

the halo is deflected away from the beam axis by a dipole "sweeping" magnet just downstream of the collimator. A secondary collimator follows the sweeping magnet to stop the deflected shower particles and block the halo of secondary photons generated by the first collimator. The secondary collimator is of a larger diameter than the primary and so sees a reduced rate of secondary interactions on the inner surface of the hole. What new showers are generated there are cleaned up by a second sweeping magnet. The beam then passes through a final collimating aperture into the experimental hall. This triple-collimation system was copied from the setup developed at SLAC [2].

The collimated photon beam, now only a few mm in diameter, is delivered to the experimental target. After passing through of order 3% radiation lengths of target, the photon beam passes through the detector and into the photon beam dump at the back of the hall. Based upon a design upper limit of 60kW (5μA at 12 GeV) being delivered to the electron beam dump, the total power in the photon beam is not more than 1.5W in the experimental hall and not more than 15W in the collimator enclosure.

4.2.1 Essential features

The adjective 'coherent' in coherent bremsstrahlung does not indicate that the photons in the beam are in a coherent state, as is light from a laser. Rather it refers to the coherent effect of multiple atoms in a crystal lattice in absorbing the recoil momentum from a high energy electron when it radiates a bremsstrahlung photon. In X-ray spectroscopy one encounters the same thing in the Mössbauer effect, except in that case the chief physical consequence is the disappearance of the recoil Doppler shift from the photoabsorption/emission spectrum. Here the chief consequence is the enhancement of bremsstrahlung at those particular kinematics for which the recoil momentum matches one of the reciprocal lattice vectors of the crystal.

Another useful way to view the process of coherent bremsstrahlung is as virtual Compton scattering. To the high energy electron, the atoms in the radiator appear as clouds of virtual photons. For a disoriented radiator material, the virtual photon spectrum is given simply by the atomic form factor, averaged over the different species in the material. If the radiator is a single crystal, however, the atomic form factor gets multiplied by the form factor of the crystal, which in the ideal case looks like a series of delta-functions located at the sites of the reciprocal lattice. In effect, the crystal provides a set of virtual laser beams, each one a standing wave tuned to a specific reciprocal lattice vector. In this view the process of hard bremsstrahlung is seen to be the same as Compton back-scattering of laser light. For a more detailed discussion of the physics of coherent bremsstrahlung there are a number of good references [2, 3, 4, 5].

The use of Compton back-scattering of laser light as a photon source was earlier noted as ruled out by the limitation of high-power lasers and cavities to wavelengths above 100 μm. The characteristic wavelength of the crystal photons is a few Angstroms, three orders of magnitude shorter. In this case, 180° scattering would result in essentially 100% of the electron beam momentum being transfered to the photon in the lab frame. However, the Compton cross section contains a factor of $1/(\vec{q} \cdot \vec{p})^2$ where $\vec{q}$ is the virtual photon momentum and $\vec{p}$ is that of the electron, which strongly favors incident photons with $\vec{q}$ nearly orthogonal to $\vec{p}$. With reciprocal lattice vectors pointing in almost every direction, only those nearly perpendicular to the beam contribute appreciably to the scattering rate. This fact applies equally to ordinary bremsstrahlung; in fact, to a first approximation the bremsstrahlung spectrum from a single crystal is the same as from a disoriented radiator. The reason is that, if the sum over crystal momenta were replaced with a continuous integral, one would recover the ordinary bremsstrahlung result for isolated atoms. Beyond

a few unit cells from the origin in reciprocal lattice space, the atomic form factor and kinematic factors become slowly varying on the scale of the lattice spacing, and the sum becomes indistinguishable from the integral. Besides that, the uncertainty principle requires that atoms localized at the sites in a crystal undergo fluctuations about their mean position. This has the effect of attenuating the discrete peaks in the crystal form factor at progressively higher-order crystal momenta, eventually washing them out and filling in the gaps between them, so that the sum deforms smoothly into the integral at high momentum transfer. Hence, the sum over crystal indices that yields the final photon spectrum can be separated into two parts: a discrete sum over a limited set of small crystal indices and an integral over the continuum of momentum transfer values beyond. The latter appears in the coherent bremsstrahlung beam as an ordinary $1/k$ bremsstrahlung spectrum, while the former appears as a set of peak structures superimposed upon it. The $1/k$ continuum, referred to as the incoherent component, is invariant as the crystal is rotated, whereas the coherent peaks change in position and intensity, depending on crystal orientation.

A typical coherent bremsstrahlung spectrum is shown in Fig. 4.5. The distinction between incoherent and coherent components in the figure is artificial; it is there to show the part of the spectrum that shifts as the crystal is rotated. The vertical scale in the figure gives the photon rate for the given beam current and crystal thickness. Note that the intensity of the incoherent background is less than what would be obtained with an amorphous carbon radiator of the same thickness, because a part of the momentum transfer integral in the Bethe-Heitler formula has been moved into the discrete sum and contributes to the coherent part. The radiation length of diamond is actually an average over all orientations of the crystal. In the calculation for Fig. 4.5 the leading 400 lattice sites were included in the discrete part of the calculation, although it can be seen that only two or three of them contribute with sufficient intensity to be individually visible in the spectrum.

4.2.2 Use of collimation

The presence of the large incoherent flux in Fig. 4.5 presents a significant handicap to a photoproduction experiment. Not only do the low energy photons produce background in the detector, but they diminish the polarization of the beam. The entire beam polarization appears in the coherent component; the underlying incoherent flux only serves to dilute the polarization. There is another difference between the two components that allows them to be separated to some extent. The kinematics of bremsstrahlung confines most of the inten-

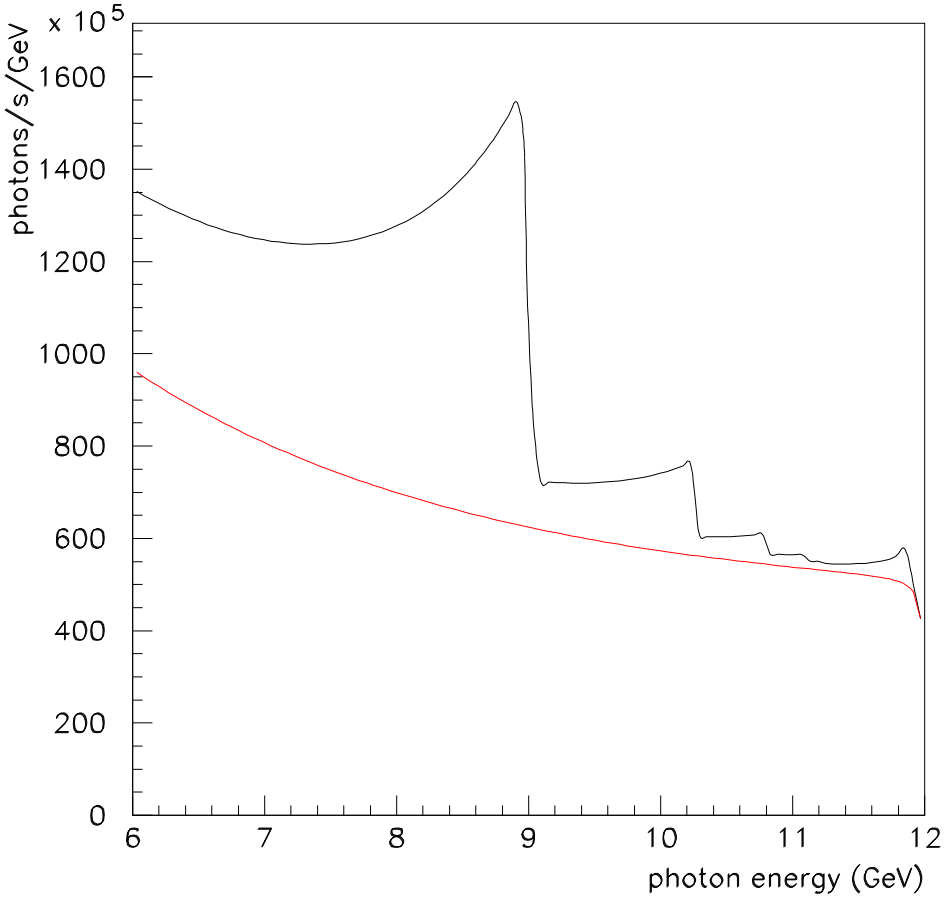

Figure 4.5: Coherent bremsstrahlung spectrum, calculated for a diamond crystal radiator 15μm thick and a 1μA electron beam of 12 GeV energy. Typical values were used for beam emittance and crystal mosaic spread.

sity of the photon beam to forward angles within m/E radians of the incident electron direction. In the lab this is a small angle, but in the rest frame of the electron-photon system it subtends all angles in the forward hemisphere. A peak in the coherent component that corresponds to a single reciprocal lattice vector has two-body kinematics, so there is a well-defined relation between the emission angle and the energy of the emitted photon in the lab: emission at 0° yields a maximum energy photon, with energy decreasing with increasing angle. This accounts for the shape of the coherent peaks in Fig. 4.5, with the sharp right-hand edge corresponding to 0° emission and the tail to lower energies corresponding to scattering into higher angles.

The incoherent component, because it comes from a sum over momentum transfers at all angles, has essentially no correlation between photon energy and emission angle. This means that collimating away all photons beyond some angle $\theta_{max} < m/E$ uniformly attenuates the incoherent spectrum at all energies, whereas it preserves all of the coherent photons from the maximum energy for the given peak down to some cutoff. The kinematic relations for coherent bremsstrahlung are as follows,

$$\theta^2 + 1 = \left(\frac{1-x}{x}\right)\left(\frac{x_{max}}{1-x_{max}}\right) \tag{4.1}$$

$$x_{max} = \frac{2\vec{p}\cdot\vec{q}}{2\vec{p}\cdot\vec{q} - m_e^2} \tag{4.2}$$

where x is the photon energy in units of the incident electron energy and θ is the lab emission angle of the photon relative to the incident electron momentum axis, in units of m/E .

The effects of collimation are demonstrated in the calculated spectra shown in Fig. 4.6. First, note that the collimation angles are very small, which requires a long flight path of order $100\,m$ in order that the collimator can be larger than the intrinsic beam spot size, otherwise the collimator is cutting in transverse coordinate instead of in angle. This distance is, in fact, a sensitive function of the electron beam emittance from the machine, and must be increased in inverse proportion to the beam emittance if the effectiveness of collimation is held constant. This issue, along with the associated demands placed on beam alignment and position stability, are taken up in more detail in the following section on the electron beam line.

Second, note that the cut imposed on the coherent peak by collimation does not produce a perfectly sharp edge as would be expected from two-body kinematics. This is because the collimator cuts on radius at some fixed distance which translates into a cut on emission angle only in an approximate way,

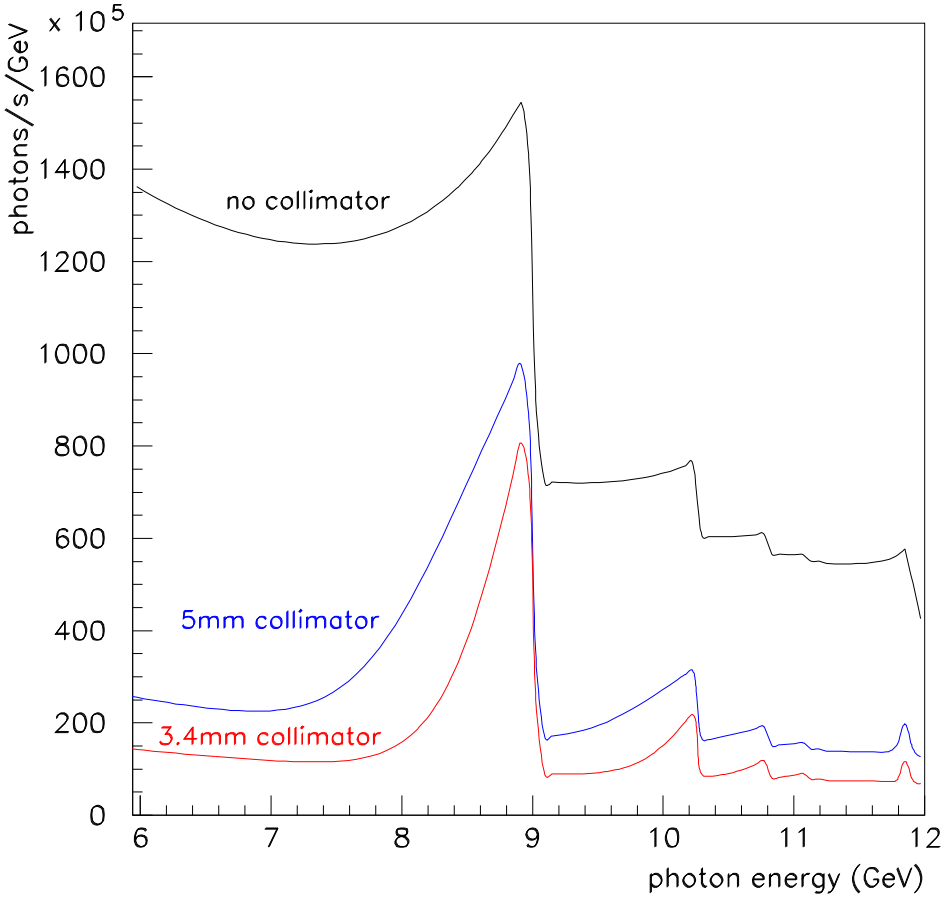

Figure 4.6: Coherent bremsstrahlung spectrum, calculated under the same conditions as in Fig. 4.5 , after collimation. The upper curve is the uncollimated spectrum from Fig. 4.5. The middle curve corresponds to a $5\,mm$ diameter collimator placed 80m downstream of the radiator, or approximately $0.75\ m/E$ in collimator half-angle. The lower curve corresponds to a 3.4mm collimator in the same position, approximately $0.50\ m/E$. For the $3.4\,mm$ collimator there are approximately $3.3 \times 10^7 \gamma/s$ in the primary peak.

thus the curves in Fig. 4.6 are labelled by their collimator size and distance individually rather than their ratio which is the nominal collimation angle. Multiple scattering by the electron in the radiator prior to emission and beam spot size and divergence are the major contributors to the error involved in translating a collimator radius into a cut on emission angle. All of these effects have been incorporated into the analytical calculation of the yields from a collimated coherent bremsstrahlung source that has been used in preparing this report. Crystal imperfections, which amount to an intrinsic spread in the direction of the incoming virtual photon, are also taken into account in the calculation.

Third, note that the relatively weak collimation at $5\,mm$ reduces the incoherent background without significantly affecting the coherent flux near the maximum, and thereby almost doubling the polarization of the beam at the peak relative to the uncollimated case. Further reducing the collimator diameter continues to narrow the peak and reduce the incoherent flux relative to the peak, albeit at some cost in peak intensity.

The $3.4\,mm$ collimator diameter has been chosen for this design because it provides for a maximum reduction in the incoherent flux while transmitting 95% of the coherent flux at the peak. Most of the net photon beam energy, however, is being absorbed by the collimator. For this reason the collimator is located in a separate enclosure outside the experimental hall, and must be surrounded by a considerable amount of shielding. The peak in Fig. 4.6 for a $3.4\,mm$ collimator contains 33M photons/s for an electron beam current of 1μA, which will be increased by a factor of 3 for full-intensity running in HALL D.

Fourth, note that the rate seen in the focal plane of the tagging spectrometer corresponds to the upper curve in Fig. 4.6, regardless of the collimation. This means that collimating the bremsstrahlung beam increases the rate in the tagger focal plane relative to what is seen at the detector. For full-intensity running at 10^8 photons/s on target in the coherent peak, Fig. 4.6 implies a rate of 240 MHz in the focal plane within a 600 MeV window around the peak. Combining this rate with the beam pulse spacing of 2ns leads to an accidental tagging rate of about 50% and to a fraction of ambiguous tags of 40%. In an ideal detector the per-second yield of single-tag events does not saturate until the fraction of ambiguous tags reaches 63%; however detector rate and trigger considerations will lower this figure somewhat. The detector and tagging spectrometer design are based upon a maximum rate of 10^8 photons/s on target and 400 MHz per GeV in the tagger. A novel focal plane design is currently under study, to be discussed below in section 4.4, which may enable the focal plane rate to be reduced by about a factor of two without any decrease in the

collimated flux.

The linear polarization of the photons in the coherent peak is shown in Fig. 4.7 as a function of the energy of the electron beam. This figure demonstrates why it is essential to have electrons of as high energy as possible, even though photon energies of no more than $9GeV$ are required. The intensity of the coherent peak, not shown in the figure, has a similar dependence on the electron beam energy in this region.

Shown in Fig. 4.8 is the linear polarization of the photon beam *vs* photon energy for fixed electron beam energy. The dashed curves show how the maximum polarization in the primary peak varies as the peak energy is changed by rotating the crystal. The polarization in all cases is zero at the endpoint. Without collimation it rises as $(E_0 - k)^2$, one power coming from the intensity of the coherent peak relative to the incoherent component going to zero linearly at the endpoint, and the other from the intrinsic polarization of the coherent photons also behaving like $(E_0 - k)$ near the endpoint. Collimation allows one to essentially isolate the coherent component, so that the polarization available to the experiment rises from zero at the endpoint in a linear fashion. The dashed curves in Fig. 4.8 demonstrate this point.

In order to obtain the full polarization enhancement from collimation, it is necessary to have a distance between the radiator and collimator on the order of $100\,m$. This distance scale is set by the requirement that the collimator aperture must be large compared to the virtual electron beam spot on the collimator but small compared to the actual photon spot size.

The size of the virtual spot at the collimator is controlled by the beam emittance coupled with a limit of 20μr on the angular spread of the electron beam at the radiator. The latter value was chosen to approximately match the spread in the beam incidence angle to the mosaic spread of the crystal because it is the combination of the two that limits the definition of the coherent peak. Taking this value together with an emittance of 10^{-8}m·r which has been projected for the CEBAF beam at $12\,GeV$ leads to a virtual spot size of $0.5\,mm$ r.m.s. ($1.2\,mm$ f.w.h.m.) Note that this scale does not depend on the radiator-collimator distance. The size of the real photon spot is given by one characteristic angle m/E which defines a circle on the collimator containing approximately 50% of the total photon intensity. The real spot size is proportional to the radiator-collimator distance. At a distance of 80m the ratio of spot sizes is 6, sufficient to allow a range of collimator sizes that satisfy both of the above inequalities.

Fig. 4.9 shows the peak polarization of the beam as a function of radiator-collimator distance for a coherent peak at 9 GeV. In this calculation the collimator diameter is held constant at $3.4\,mm$ to make sure that the virtual

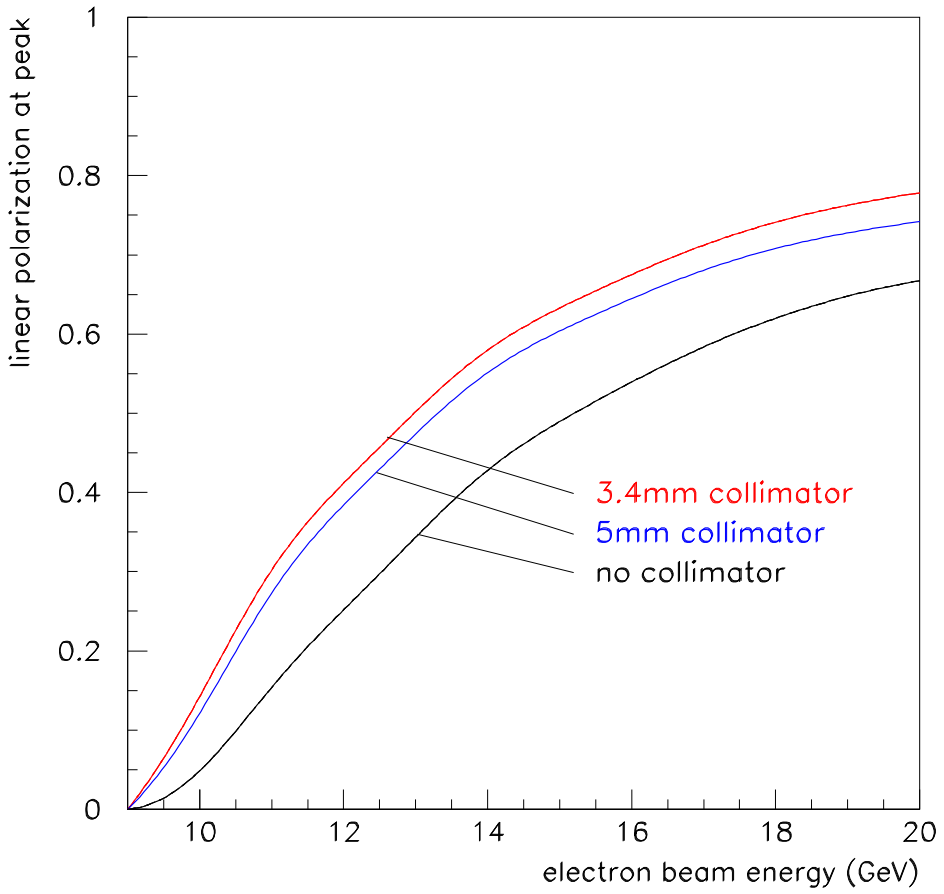

Figure 4.7: Linear polarization in the coherent bremsstrahlung peak as a function of electron beam energy keeping the energy of the coherent peak fixed at $9GeV$. The calculation is performed under the same conditions as in Fig. 4.6.

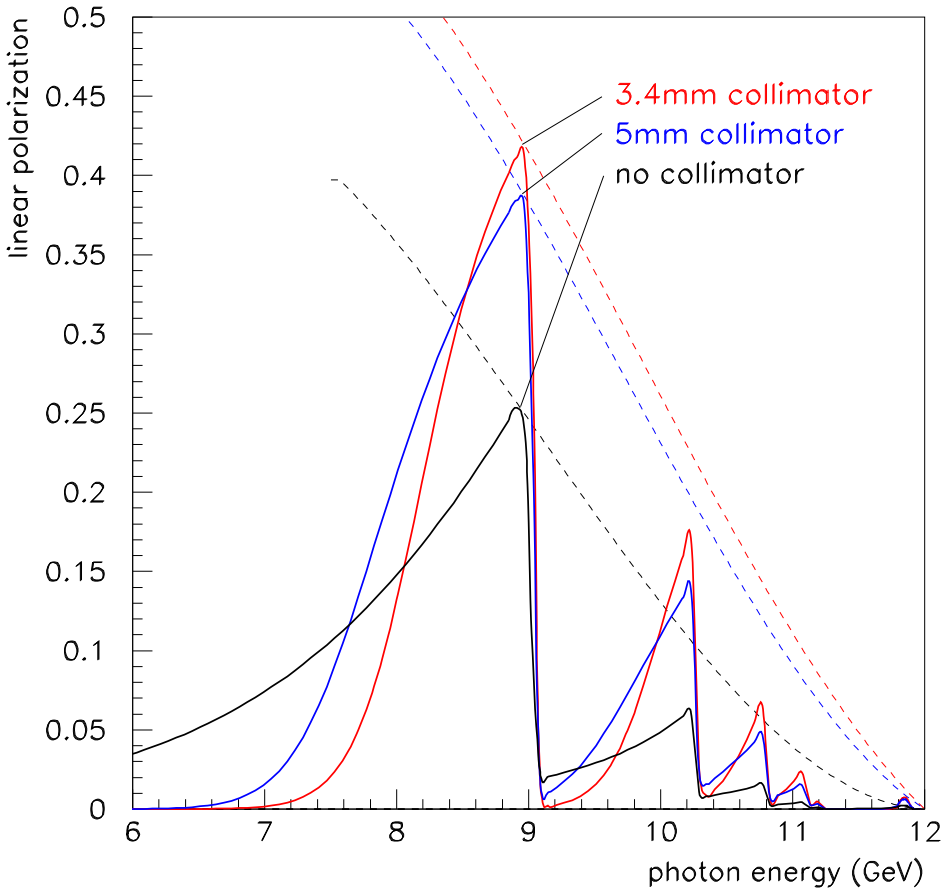

Figure 4.8: Linear polarization of the coherent bremsstrahlung beam for a fixed electron beam energy of $12GeV$ calculated under the same conditions as in Fig. 4.6. The dashed lines indicate the trajectory of the peak polarization as the peak energy is swept across the focal plane by rotating the crystal.

beam spot of 1.2 mm f.w.h.m. is well-contained, which is the main condition for effective collimation. At zero distance the collimator has no effect except to attenuate the beam, and so the uncollimated polarization from coherent bremsstrahlung is obtained. At 100m separation distance the polarization enhancement from collimation has saturated. The design for HALL D calls for a radiator-collimator distance of approximately 80 m. However from the figure one can see that the performance of the photon source is not a very sensitive function of this variable.

4.2.3 Choice of radiator

The ideal radiator would be a layered structure with strong transverse fields that alternate between layers spaced about 50 nm apart, thus simulating the standing wave in a cavity driven by a 15 eV laser. While it is possible to construct ordered materials with unit cells as large as this, the self-shielding of atoms means that beyond the atomic length scale the residual fields are comparatively weak. Hence heterogeneous structures are not viable for use as a coherent radiator. Since the strong fields inside a solid are revealed at the atomic scale, the first requirement for a good radiator is that the unit cell be compact and closely packed. The best radiators are those with the smallest unit cells because these provide the best match between the atomic and the crystal form factors. This match is best for the light elements, and essentially prohibits the effectiveness of any materials heavier than carbon. An extensive survey of possible radiator materials is presented in Ref. [3]. In Table 4.1 is shown the figure of merit that those authors report for favored crystalline materials. The figure of merit is the product of the atomic times the crystal form factor evaluated at the leading peak, normalized to the value for diamond.

Table 4.1 shows that the list of viable materials for a crystal radiator is relatively short. Silicon would be an excellent choice from the point of view of price and fabrication, but unfortunately it is far inferior in terms of performance. Beryllium carbide is not a material that is familiar to the crystal growth industry, and nothing is known at present concerning its suitability for the growth of single crystals of large area. In general compound materials are more susceptible to radiation damage than are pure elements, which would argue in favor of diamond and beryllium metal. These two materials are comparable in terms of their performance.

Most of the experience to date with coherent bremsstrahlung has been with diamond radiators. Extensive expertise for handling large diamond crystals exists within the gem industry. Recently, since it has become necessary to find

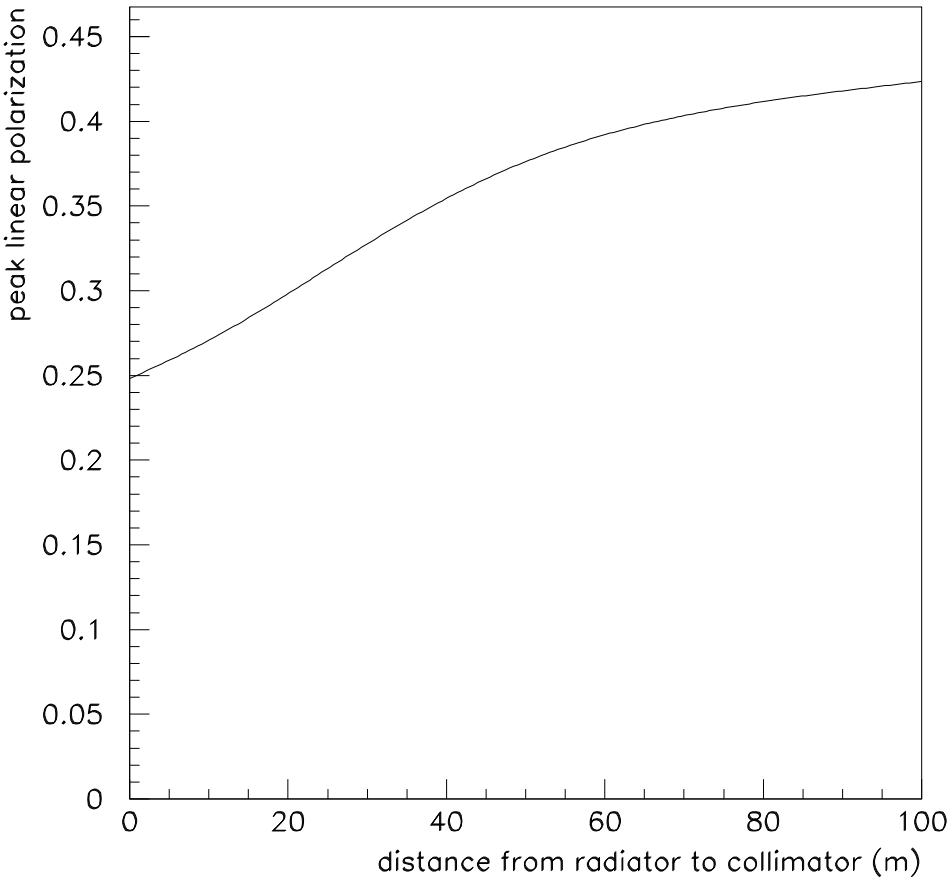

Figure 4.9: Maximum polarization *vs* radiator-collimator distance for a coherent peak at 9 GeV. The collimator diameter is held fixed in this calculation to keep a constant ratio between the sizes of the virtual electron spot and the collimator.

crystal	best reciprocal vector	$P/P_{diamond}$
diamond	2,-2,0	1.00
beryllium	0,0,2	0.86
boron	2,0,8	0.38
silicon	2,-2,0	0.19
Be_2C	2,2,0	1.10

Table 4.1: Figure of merit of various materials that might be used as a coherent bremsstrahlung radiator. This table is reproduced from Table 2 in Ref. [3].

some new diamond radiators for the coherent bremsstrahlung tagged photon facility in Mainz, members of the Glasgow group have established good contacts within the gem industry for procuring diamonds, and have developed techniques for assessing the quality of the diamonds [6].

Currently, there is a need for diamonds with areas greater than 5mm $\times$ 5 mm for X-ray windows on synchrotron light sources. Ideally, the diamonds should have a perfect crystal structure. In general terms, diamonds are classified as type I or type II, where type II have been subjected to greater stresses during their formation than type I. Commonly, type II exhibit substantial plastic deformation. Diamonds are also classified according to the form in which nitrogen atoms are present in the crystal lattice. In type a the nitrogen is aggregated into clusters of atoms, whereas in type b the nitrogen is almost uniformly distributed throughout the crystal. For coherent bremsstrahlung radiators, type Ib diamonds are the most suitable. Unfortunately, type Ib natural diamonds are very rare and probably the most reliable source of Ib diamonds will be synthetics. At present synthetic diamond monocrystals typically have nitrogen concentrations around 100 ppm.

Synthetic diamonds are made using either vapour deposition (CVD) or high pressure high temperature (HPHT) techniques. CVD diamonds have an extensive mosaic and are unsuitable for coherent bremsstrahlung. However HPHT synthetics look very promising, and the Glasgow group have recently acquired a 5 mm $\times$ 5 mm synthetic diamond less than 18μm thick which has a [100] orientation. It produces a very good coherent bremsstrahlung spectrum and X-ray measurements show it has rocking curve widths of less than 10μr, quite close to the ideal value for diamond.

Beryllium is another material that might be used as a crystal radiator. Beryllium metal is widely used in industry, being preferred for its high strength-

to-weight ratio and robustness, in addition to its transparency to X-rays. Thin films of high-purity beryllium are routinely produced for vacuum window applications, which use some of the same vacuum deposition techniques that would be used for the growth of single crystals. As a radiator material, beryllium is distinguished as the metal with the highest Debye temperature, around 1400°K . The Debye temperature measures the temperature at which the thermal motion of the atoms in the lattice reaches the level of the zero-point motion due to their confinement in the lattice, as dictated by the uncertainty principle. A high Debye temperature indicates a stiff crystal lattice, in which the atoms have little liberty to move and so have large momentum fluctuations, as dictated by the uncertainty principle.

A high Debye temperature is important for a bremsstrahlung radiator material for three reasons. First, the cross section for coherent bremsstrahlung from a discrete crystal momentum vector $\vec{q}$ contains a factor $e^{-q^2/4M\theta_D}$ which reflects the fact that position fluctuations of atoms in the lattice diminish the coherent effect. This factor is near unity for the low-order crystal momenta provided that θ is sufficiently large. Second, the Debye temperature is, roughly speaking, a measure of the stability of the crystal structure and hence its readiness to form as a single crystal and to survive significant doses of radiation. Third, the radiator material will inevitably be heated by the beam, and will normally operate in vacuum well above the ambient temperature. A high Debye temperature means that there is a large range of temperatures over which the material may operate without degraded performance as a crystal radiator. The Debye temperature of diamond is about 2200° K. Past experience has shown that diamond meets all of the requirements for a good crystal radiator.

Beryllium remains therefore a second choice, to be investigated further in the case that affordable sources of large-area diamond crystals at some point are no longer available. The growing need for such crystals for use at synchrotron light sources gives reason for confidence that this is not likely to happen any time soon.

4.2.4 Crystal thickness

The range of permissible thicknesses for a crystal radiator is bounded both from above and below. It is bounded from above by multiple scattering of the electron beam as it passes through the radiator, which causes the divergence of the incident beam to grow, thereby enlarging the photon beam spot on the collimator face and degrading the degree to which collimation discriminates against the incoherent component in favor of the coherent part. It is bounded from below by the fact that the crystal must be of some minimum thickness

in order to achieve the full coherent gain. In the calculation of the coherent bremsstrahlung process one begins by assuming an infinite crystal, although practically it is presumed to mean only that the crystal is large compared to the some characteristic scale. It is important to identify what the characteristic scale is in this problem in order to know how thin one can make the crystal without hurting performance. In the analogous case of the Mössbauer effect, one can estimate the number of atoms participating in the collective absorption by looking at the emission time of the photon (lifetime of the radiating transition) and asking how many nuclei lie within the envelope of the photon wave packet. In the coherent bremsstrahlung process, the lifetime of the radiating system is given in the lab system by the uncertainty principle and by how far the electron energy deviates from its on-shell value between absorbing the virtual photon and emitting the real one. The latter quantity is almost exactly given by q_z , the virtual photon momentum component along the incident electron axis, which means that the electron travels a distance $\lambda = \hbar c/q_z$ during the interaction. For a given coherent peak at normalized energy x in the photon spectrum, the coherence length is given by

$$\lambda = \frac{2E(1-x)}{xm^2} \tag{4.3}$$

in units of $\hbar c$. From this simple argument one sees that the coherent gain goes linearly to zero at the endpoint, a result that is borne out by the full QED calculation. One also sees that the lower limit on crystal thickness imposed by the coherence length depends upon both the electron beam energy and the photon energy. For a 12 GeV beam energy and a 6 GeV coherent photon the coherence length is 18 nm, or about 50 unit cells for diamond. This shows that the coherence length does not impose a practical limit on how thin the radiator should be.

The effects of multiple scattering are best presented by showing the calculated spectra for various radiator thicknesses. In Fig. 4.10 is shown the photon spectrum for a 10^{-4} and a 10^{-3} radiation-lengths radiator to demonstrate the effect. The 10^{-3} radiator spectrum is scaled down by a factor of 10 to facilitate the comparison. The calculation assumed a 3.4 mmcollimator located 80 m downstream of the radiator. The loss in normalized intensity with the thicker radiator, as well as the broadening of the left edge of the peak, is due to the enlarging of the photon beam spot on the collimator face from multiple scattering of the electron beam in the crystal prior to radiation. A 10^{-4} diamond radiator is 15μm thick. The goal for HALL D is to run with crystals of thickness in the range 10μm to 20μm.

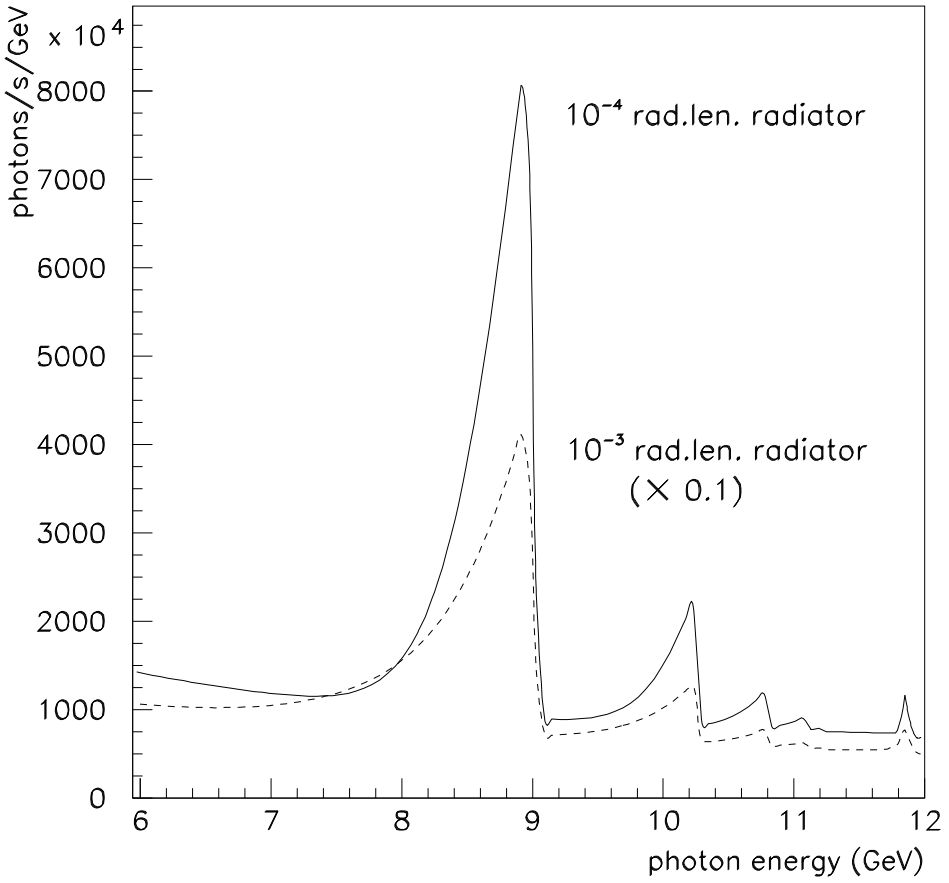

Figure 4.10: Collimated coherent bremsstrahlung spectrum from a 1μA electron beam at 12 GeV using diamond radiators of two different thicknesses. The calculation assumes a 3.4 mmcollimator located 80 m from the radiator, and typical values for beam emittance and crystal quality.

Axis	Motion	Range	Step size
x	horizontal translation	-50 mm – +50 mm	0.01 mm
y	vertical translation	-20 mm – + 20 mm	0.01 mm
θ_v	vertical rotation	-100mr – +100mr	10μr
θ_h	horizontal rotation	-100mr – +100mr	10μr
ϕ	azimuthal rotation	-100° – +100°	0.01°

Table 4.2: Requirements for goniometer axes

4.2.5 Crystal mount

It has already been shown that in order to achieve appreciable coherent gain the crystal must be oriented so that the coherent peaks appear well below the end point. Eqn. 4.2 then implies that the orientation must be such that the crystal momentum dotted with the beam momentum be of order m^2 . Given a p of 12 GeV and q of 10keV, this requires that the two vectors must be within 100μr of perpendicular to each other and that, within a range of angles of that order, the coherent peak sweeps out nearly the full range in x from 0 to 1.

Hence, to have a stable photon beam with the coherent peak positioned at the right energy, the angle between the incident electron beam and the crystal radiator must be adjustable in steps of a few μr and remain stable at this level. Since the angle of the incident beam is fixed by the beamline optics and the position of the photon collimator, all adjustments must be made by changing the orientation of the crystal. This is achieved with a precision goniometer (shown schematically in Fig. 4.11) which should provide motion on at least 5 axes. Rotation about the azimuthal axis ϕ sets the orientation of the polarization plane, rotations about the θ_v, θ_h axes set the angle of the crystal relative to the beam, and x, y translations select the position of the beam spot on the crystal. Estimates of the approximate range and step size for each of the axes are given in table4.2.

In practice several targets need to be mounted in the goniometer. The minimum requirement is a diamond crystal, an amorphous radiator, and a blank. It is also desirable to have a screen to show the position of the beam spot and a spare diamond. This means either mounting some targets off-axis on the azimuthal plate (as in the Mainz setup), or having a sixth axis to allow a target ladder to sit inside the azimuthal plate (as in the Jlab Hall B setup). A goniometer with the required precision can be obtained commercially, and would be controlled with the slow control system.

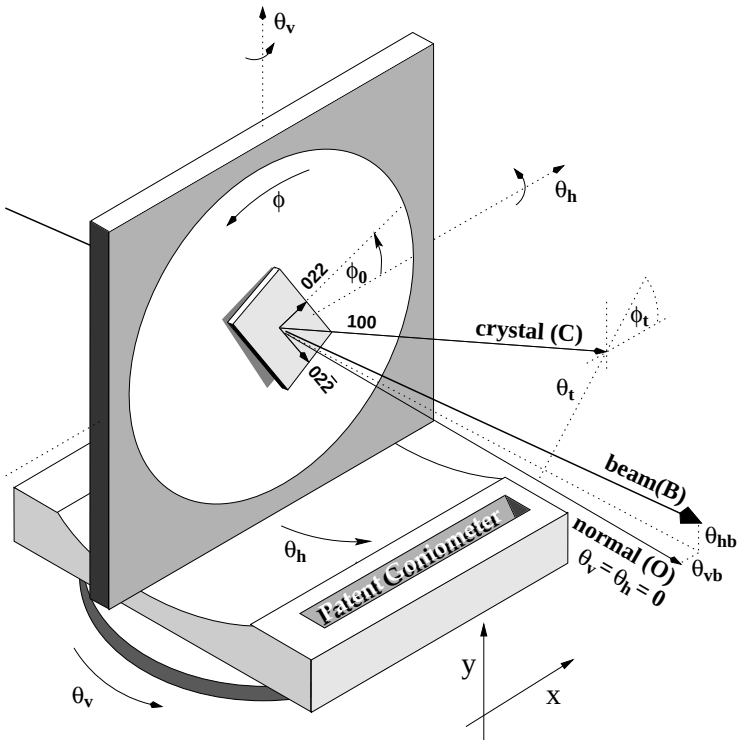

Figure 4.11: Schematic illustration of crystal mounted in goniometer

4.2.6 Crystal alignment and monitoring

As can be seen in Fig. 4.11 the goniometer setting θ_v,θ_h defines the direction of the normal to its inner plate (O). Ideally at its zero setting $\theta_v = \theta_h = 0$ this would coincide with the electron beam direction (B), but in practice there are small offsets θ_{vb}, θ_{hb} which may vary according to the stability of the electron beam. There will also be a misalignment of the crystal lattice with respect to the inner plate due to imperfections in the mounting and in the cutting from the original stone. The 100 axis (C) will be tilted with respect to the inner plate at an angle θ_t with this maximum tilt occurring at an azimuthal angle ϕ_t. In addition, the 022 vector will be offset by ϕ_0 with respect to the horizontal. Any motion about the azimuthal axis ϕ changes the angle of the 100 axis (C) relative to the beam. The angle of the polarization plane is set by adjusting the azimuthal angle of the crystal ϕ. Hence when a new crystal is installed, the default value ϕ_0 needs to be measured. Furthermore, to position the coherent peak at the required photon energy, the angle (or *offsets*) between the beam and 100 crystal axis (C) at the chosen value of ϕ must also be established.

Feedback on the relative angle between the crystal and the beam is obtained from a photon energy spectrum derived from the tagger focal plane counters, either via scalers or a TDC hit pattern. The scaler spectrum does not show the effect of collimation (unless the scalers are gated with a downstream photon detector), but can be obtained very quickly since it does not require a triggered data acquisition system. The scaler readout is essential for the alignment process, where the offsets are measured by carrying out a series of scans in which 2d histograms of photon energy vs. crystal angle are built up by moving the goniometer in a sequence of small angular steps and reading the tagger scalers. In addition to providing the feedback required for alignment, the focal plane counters provide essential online diagnostics to monitor drifts in angles caused by the beam tuning, or thermal effects in the crystal mount. If necessary a feedback system could be implemented via the slow control system, where any drift in the position of the coherent peak could be corrected by periodically adjusting the goniometer within predefined limits.

The spectrum obtained from the tagger focal plane can also provide online monitoring of the photon polarisation to within 5% by fitting with an analytic bremsstrahlung code.

4.2.7 Crystal quality and lifetime

There are two considerations that fall under the heading of crystal quality. The first respects the quality of the original crystal, and the second is with regard

to degradation from radiation damage. In the calculation of the coherent bremsstrahlung spectrum a perfect single crystal was assumed, but even the very best crystals have some dislocations and other defects. Besides locally disrupting the regularity of the crystal, these defects impose stresses which produce small ripples in the crystal planes. If these ripples were amplified, the surface of a crystal would appear like a mosaic of planar regions with approximately parallel surfaces. The scale of deviations from planarity across the face of a single crystal is termed the *mosaic spread* of the crystal. The mosaic spread contributes in the same way as beam divergence to the smearing in the exact energy-angle relation for coherent photons.

In section 4.2.3 it was mentioned the Glasgow group have developed techniques for assessing the quality of diamond radiators. Two stages are involved. Firstly the diamonds are examined under a microscope with polarized light. This reveals any stresses in the crystal lattice and is particularly useful for eliminating diamonds with plastic deformation. Then any diamond which looks as if it could be used as a radiator is examined with one of the X-ray beams from the Synchrotron Radiation Source at Daresbury in England. Three types of measurements are performed.

i. Rocking curves widths which, for a selected set of crystal planes, measure quantitatively how any defects or dislocations distort the crystal lattice. Using rocking curves it is possible to measure how close to ideal is the lattice structure of the diamond being investigated. At Daresbury, the X-ray beam can be collimated so that an area as small as $0.25\,mm$ * $0.25\,mm$ can be sampled.

ii. Projection topographs which reveal any large-scale imperfections in the crystal. Here the diamond is set at the Bragg angle for a particular set of planes and a photograph is taken of the scattered X-rays. It is possible to sample the whole volume of the crystal, and the photograph will reveal dislocations, growth boundaries and any feature which prevents Bragg scattering at the selected angle taking place.

iii. Section topographs which show the depth profile of the imperfections of the crystal. By collimating the X-ray beam to a narrow strip a few μm wide, the effects of dislocations and boundaries within the lattice through the thickness of the diamond can be examined. Hence, by measuring projection and section topographs, a 3-dimensional picture of the diamond can be obtained. It is also possible to differentiate between screw and edge dislocations.

These techniques were used to examine a diamond which had been used at Mainz for several years for providing linearly polarised photons. The electron beam on the diamond had a diameter of about 100μm and it was estimated around 10^{20} electrons had passed through the diamond. There was a small greenish black spot where the beam had hit the diamond.

The X-ray rocking curve measurements showed that considerable damage had occurred to the integrity of the crystal structure in the center of the beam spot. However $2\,mm$ away from the damage center, the width of the diffraction peak was the same as it had been for the pristine crystal, which indicates that the lifetime of the crystal could be extended by occasionally moving the beam spot on the face of the crystal.

At Mainz the area of the beam spot on the radiator is two orders of magnitude smaller than what is being planned for Hall D. A larger spot means a longer crystal lifetime before radiation damage substantially degrades its crystal properties. Appropriately scaled, the exposure of the Mainz crystal would correspond to 15 straight years of running in Hall D at the full intensity of 3μA without a spot move. Plans for the Hall D source are to keep the exposure about three orders of magnitude less than this. The SLAC group found that the performance of their diamonds had degraded noticeably after a total charge of 3 Coulombs had been accumulated over a spot of size roughly $2\,mm$ r.m.s., leading to a limit of about 0.25 Coulomb/mm^2. Taking this as a conservative estimate for the allowed exposure, the source can run at a full intensity of 3μA for 60 hours before it is necessary to move the spot on the crystal. If it had no bad zones, a square crystal of $5\,mm \times 5\,mm$would accomodate 5 spot moves before the crystal would need to be replaced. SLAC researchers were able to recover a good performance for the damaged crystals by putting them through an annealing process. Further research and development will be required to determine whether this is an effective way of reducing the operating costs of the Hall D source.

Another issue to be addressed is that of heat dissipation for very thin crystals. The heat comes from the ionization energy loss of the beam as it passes through the crystal. Although this is small compared to the bremsstrahlung energy loss, it is not entirely negligible at these beam currents. It can be calculated using the restricted energy loss formula, which yields 21mW for a 15μm (10^{-4} radiation lengths) crystal at a current of 3μA. This is not much power, but the crystal is very thin. Heat dissipation is through radiation and conduction. Diamond has a very high melting point; at low pressures it sublimates at about 4027^oC. However at normal pressures it begins to transform into graphite above 707^oC, at a rate that depends on temperature. It is therefore important that the crystal at the center of the beam spot stay well below

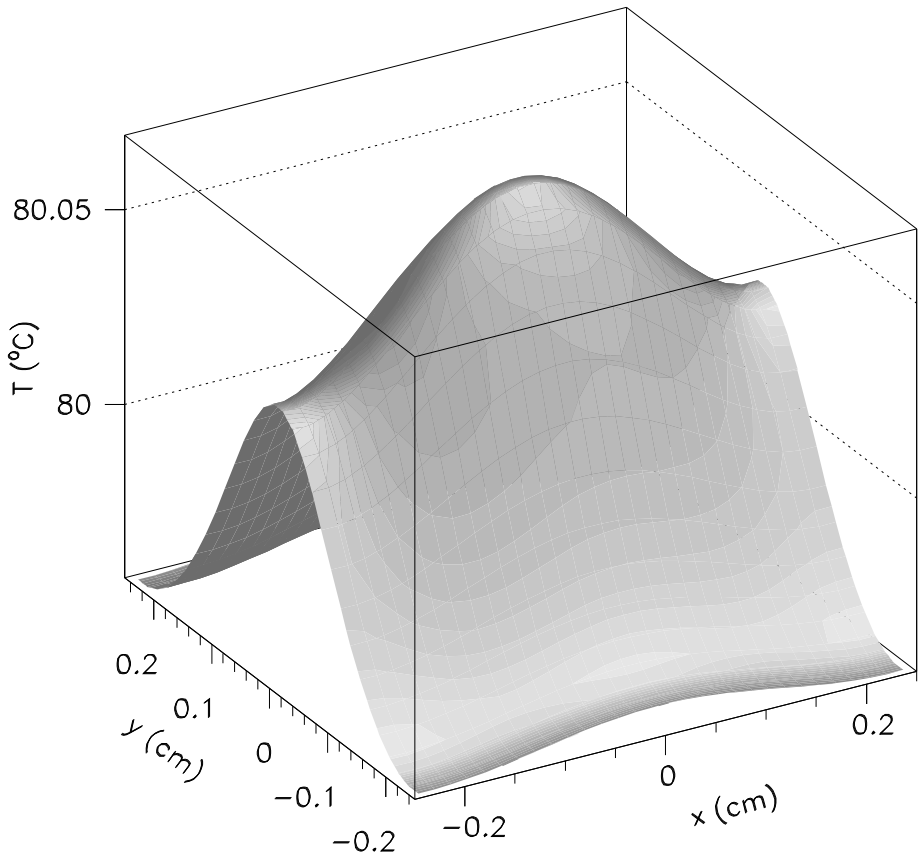

Figure 4.12: Calculated temperature profile of diamond crystal with a 12 GeV beam at 3μA. The crystal dimensions are 5 mm × 5 mm × 15μm. The ambient room temperature was taken to be 27^oC (300 K).

this limit.

The diffusion equation including a heating term and one for radiative cooling can be written as

$$C_P\, a\, \frac{dT}{dt} = h(x,y) - 2\sigma\left(T^4 - T_0^4\right) + \kappa\, a \nabla^2 T$$

where the heating term $h(x,y)$ has units of power/area, σ is the Stefan-Boltzmann constant, C_P is the heat capacity and κ the coefficient of conduction for diamond, and a is the thickness of the crystal. T_0 is the ambient temperature of the environment and T is the local crystal temperature, a function of space and time coordinates. After a certain time, T converges to the steady-state solution shown in Fig. 4.12. The calculation used a crystal of dimensions $5\,mm \times 5\,mm \times 15\mu$m and a beam current of 3μA. This calculation shows that the conductivity of diamond is sufficient to prevent significant temperature gradients across the crystal even for very thin wafers, and that radiative cooling alone is sufficient to dissipate the heat being generated by the beam passing through the crystal so that the crystal mount does not need to act as a heat sink.

4.3 Electron Beam

The performance of the photon source is dependent upon the parameters of the electron beam in several important areas. These parameters are listed in Table 4.3. The first column of numbers gives the set of parameters that have been adopted as the design goals for the source. These are the values that have been taken as input in calculating the characteristics of the coherent bremsstrahlung source for HALL D. The second column of numbers were obtained from a concrete design of the HALL D beam line [7] that was carried out by members of the Jefferson Lab Accelerator Division. The exact choice of the final parameters has not yet been made, but the preliminary design shows that all of the design goals can be met within the available real estate.

The following sections highlight the particular properties of the electron beam which have a special impact on the performance of the source.

4.3.1 Beam polarization

It has already been stated that to generate bremsstrahlung photons with linear polarization it is necessary to use an oriented crystal radiator. However photons with circular polarization are produced by ordinary incoherent bremsstrahlung any time the incident electrons are longitudinally polarized. In fact

parameter	design goals	design results
energy	12 GeV	12 GeV
electron polarization	not required	unknown
minimum useful current	100 pA	100 pA
maximum useful current	3 μA	3 μA
r.m.s. energy spread	< 10 MeV	7 MeV
transverse x emittance	10 $mm{\cdot}\mu$r	10 $mm{\cdot}\mu$r
transverse y emittance	2.5 $mm{\cdot}\mu$r	2.3 $mm{\cdot}\mu$r
x-dispersion at radiator	none	negligible
y-dispersion at radiator	none	$<$ 1cm
x spot size at radiator	1.7 mm r.m.s.	1.55 mm r.m.s.
y spot size at radiator	0.7 mm r.m.s.	0.55 mm r.m.s.
x image size at collimator	0.5 mm r.m.s.	0.54 mm r.m.s.
y image size at collimator	0.5 mm r.m.s.	0.52 mm r.m.s.
distance radiator to collimator	80 m	80 m
position stability	± 200 μm	

Table 4.3: Electron beam properties that were asked for (column 2) and obtained (column 3) in a preliminary optics design for the transport line connecting the accelerator to the HALL D photon source.

for 9 GeV photons produced by 12 GeV electrons, the polarization transfer from electron to photon beam is almost 90%. This raises the question of what happens when one has longitudinally-polarized electrons incident on an oriented crystal radiator. What happens in this case is that the photon beam is elliptically polarized; it carries both circular and linear polarization. There is a sum rule that limits the sum of the squares of the linear plus circular polarizations to be no greater than 1. Hence one sees the linear polarization in coherent bremsstrahlung going to zero as one approaches the end-point energy (see Fig. 4.8) while at the same time the circular polarization goes to 1 at the end-point (assuming electrons of 100% longitudinal polarization).

Thus the statement in Table 4.3 that electron beam polarization is not required for HALL D is correct, but it is not correct to assume that the photon source is independent of the state of polarization of the electron beam. The presence of a non-zero circular polarization in the HALL D photon beam will, in principle, produce observable effects in the angular distributions measured in photoproduction reactions. This means that there will be an important coupling between the HALL D program and the other experimental halls whose programs sometimes require them to have control over the beam polarization. This coupling can be eliminated by setting up the tune of the electron beam line to HALL D such that the longitudinal component of the electron beam polarization is rotated to zero at the crystal radiator. Whether the decision is made to rotate it away or simply to measure its value periodically, this consideration underlines the importance of having a means to measure photon beam polarization in a way that does not rely on *a priori* knowledge of the properties of the electron beam.

Although the ability of the source to produce photon beams with both circular and linear polarization complicates operation when one of them is desired without the other, it does increase the versatility of the source. The two kinds of polarization are controlled independently of one other, and together they give access to a more complete set of polarization observables than would be possible with only one or the other.

4.3.2 Beam emittance

The values for the electron beam emittances shown in Table 4.3 are estimates based upon the parameters of the current machine projected to 12 GeV[7]. The definition of emittance used here is the product of the r.m.s. widths of the beam in transverse position and divergence angle. Because synchrotron radiation inside the accelerator occurs mainly in the horizontal plane , the emittance values in x are generally larger than those for y. The two vertical

bends required for bringing the 12 GeVbeam from the level of the accelerator up to beam height in HALL D do increase the vertical emittance a small amount over its value inside the machine; this effect has been included in computing the vertical emittance shown in Table 4.3.

The longitudinal emittance of the beam is important as it is the limiting factor in determining the ultimate energy resolution of the tagger. The design goal of 0.1% photon energy resolution is well matched to the energy spread expected for the CEBAF beam at 12 GeV.

The place where transverse emittance plays a critical role is at the photon collimator. For optimum effectiveness in collimation it is important that the electron beam spot at the collimator position be as small as possible. The electron beam does not actually reach the photon collimator, being bent into the dump by the tagger magnet shortly after the radiator . But considering the optics of the electron beam as if the tagger dipole were switched off, the electron beam at the radiator can be projected forward to form a virtual image on the collimator entrance plane. The position and size of this virtual spot determines the definition of 0° emission angle for the photons. If this spot is small compared to the collimator aperture and is correctly centered then the bremsstrahlung photons of a given emission angle α intersect the entrance plane of the collimator in a well-defined ring of radius $D\alpha$ concentric with the collimator aperture, where D is the distance between the radiator and the collimator entrance plane. In this way a collimator of diameter d passes only those photons of emission angle $\alpha \leq d/2D$. If however the size of the virtual spot is comparable to or larger than the collimator aperture then the ring image of photons of a given emission angle α is smeared out, so that the effect of collimation is simply to reduce the intensity of the pre-collimated beam but not to enhance the coherent component.

Note that this analysis does not place any specific limits on the size of the beam at the radiator. The beam spot can and should be larger there to increase the lifetime of the crystal between spot moves. For the SLAC coherent bremsstrahlung source the beam spot at the radiator was about 3 mmr.m.s. focused down to a 1 mmr.m.s. virtual spot at the primary collimator positioned 91 m downstream of the radiator.

The superior emittance characteristics of the CEBAF beam allow the transverse dimensions to be somewhat smaller than this for the HALL D source, more so in the vertical than the horizontal dimension. The difference between the horizontal and vertical emittance of the CEBAF beam implies that making the spot round at the radiator implies an elliptical virtual spot at the collimator, and *vice versa*. The collimator aperture is circular, so the choice was made to make the virtual spot round. This is why the beam spot on the radiator is

asymmetric.

Figure 4.13 shows how the collimated photon spectrum depends upon the transverse emittance of the electron beam. To generate this plot the increases in emittance were simply translated into an increased virtual spot size on the collimator. This was done because it was assumed that the spot size of the electron beam on the radiator, already close to $2\,mm$ r.m.s., cannot be further inflated and stay contained within the limits of the crystal. When the virtual spot size becomes comparable with the collimator aperture then the collimation is rendered ineffective, and the photon spectrum and polarization revert to their uncollimated values. There is another connection between focal spot size and beam emittance that is connected with the requirement that all electrons enter the radiator at the same incidence angle with respect to the planes of the crystal. Practically, the divergence does not broaden the coherent peak provided that it is kept below the mosaic spread of the crystal. A conservative value for the allowable angular divergence δ in the electron beam at the radiator would then be 20μr . Taken together with a 500 μm r.m.s. spot size at the focus, this leads to an emittance of 10 $mm{\cdot}\mu$r at 12 GeV. This corresponds to the upper curve in Fig. 4.13.

4.3.3 Electron beam line optics

Translating the beam emittance into a r.m.s. values for the beam radius and divergence requires the knowledge of the β function of the transport line between the accelerator and the radiator. Beta is defined as the ratio of the r.m.s. beam size to its angular divergence.

The preliminary optics design [7] of the HALL D beam line (see Table 4.3) is shown in Fig. 4.14. The horizontal and vertical beta functions are shown in the upper and lower panels, respectively. Between the two panels is shown a schematic of the transport lattice. The design begins at the exit of the beam from the end of the linac and ends at HALL D. The Z coordinate is measured along the axis of the linac, with its origin at the mid-point of the accelerator. Fig. 4.15 shows the beta functions translated into r.m.s. beam size and shifted to place the radiator at the origin. The design allows the ratio of the spot sizes at the radiator and collimator to be adjusted over about an order of magnitude simply by changing the current in the beam line elements. In this way it will be possible to optimize the optics for a given size of crystal and collimator after beams are delivered to the hall, and more precise values for the emittances are in hand.

Not only must the virtual electron spot be small enough to fit within the collimator aperture, but it must also be centered on the aperture and stable.

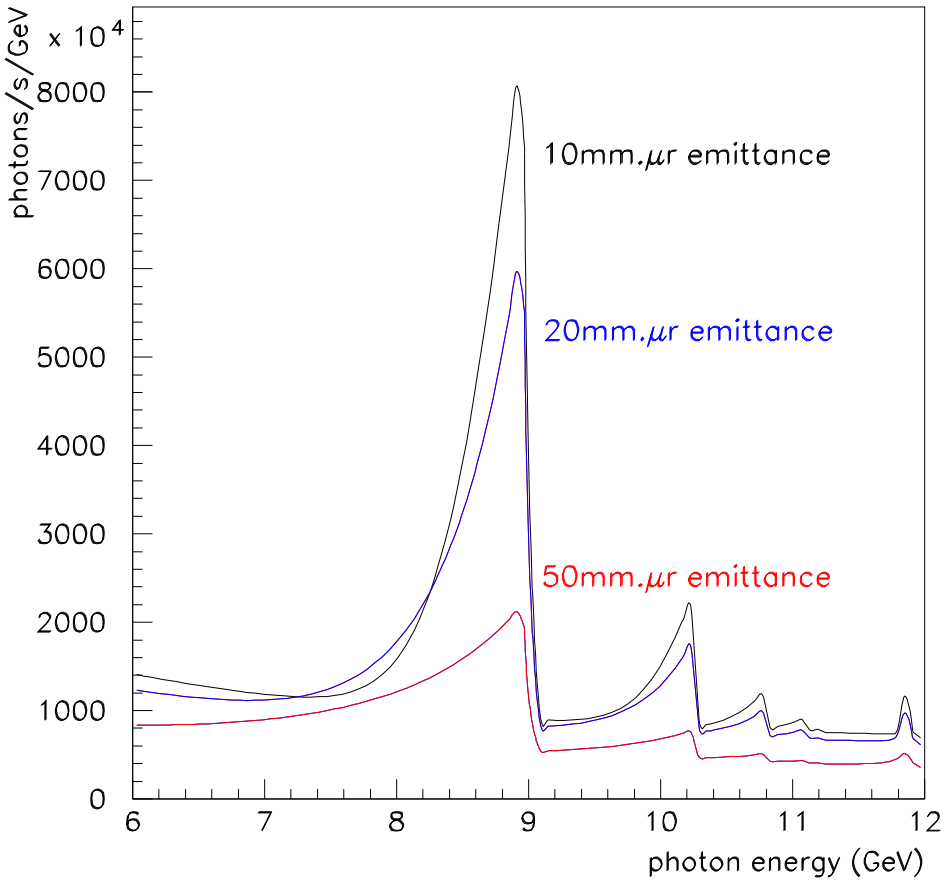

Figure 4.13: Coherent photon spectrum for three different values of the electron beam transverse emittance. The horizontal (shown on the plot) and vertical emittances are assumed to scale together. A 3.4 mm collimator located 80 m from the radiator was used for this calculation.

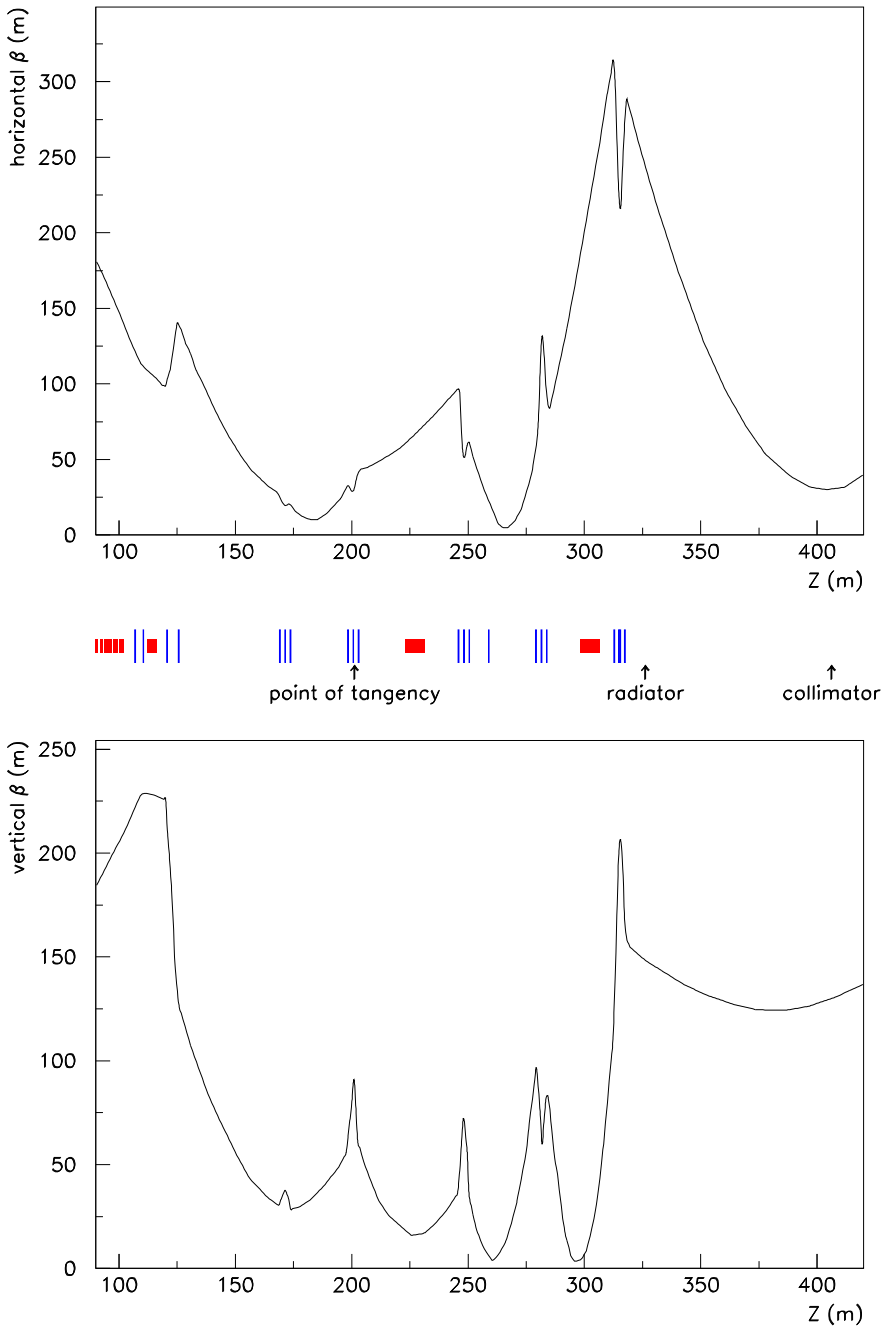

Figure 4.14: Horizontal (upper panel) and vertical (lower panel) beta functions from the preliminary optics design for the transport line from the accelerator to the HALL D photon source. The beam line lattice is shown schematically between the two panels, with dipole magnets represented by the short boxes and quadrupoles by the taller lines. The Z coordinate is equal to the flight path length of the electrons starting at the center of the linac, up to an error of a few cm from the vertical motion of the beam.

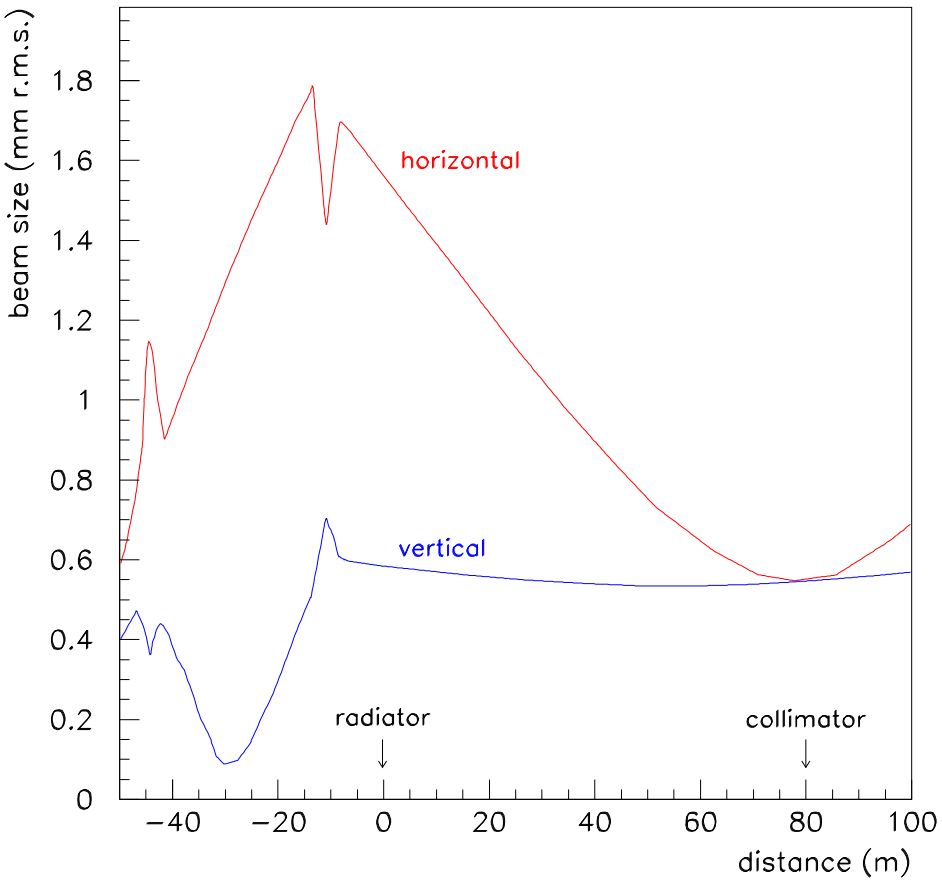

Figure 4.15: Horizontal and vertical r.m.s. envelopes for the electron beam in the region of the photon source, as derived from the beam emittance and beta functions of Fig. 4.14. The origin of the Z coordinate has been placed at the radiator. In the region between the radiator and the collimator the envelope refers to the projected image of the electron beam, and does not describe the size of a physical beam that exists in that region.

In order to maintain a stable beam position on the collimator, the SLAC experiment [2] instrumented the collimator with a secondary-emission detector (SEQ). The detector was of the "pin-cushion" design and was installed as a segment of the collimator near the position of the shower maximum. The readout was divided into four quadrants, which read equal currents when the beam was properly aligned on the collimator. The SEQ was connected via a feedback loop to the last steering elements on the electron beam line prior to the radiator. From that distance a bend of only $10\mu r$ results in a shift of $1\,mm$ at the collimator position. Hence the beam alignment feedback system is effectively decoupled from the crystal orientation controls.

The small deflections that are necessary to keep the beam centered on the collimator do not produce appreciable walk in the beam-crystal angle. This means that an active feedback system can be set up between the instrumented collimator and deflection coils just upstream of the radiator, that can operate independent of the crystal alignment system to keep the electron beam aimed at the center of the collimator.

The experimental program in parity violation at Jefferson Lab has already demonstrated a position stabilization circuit that is able to keep the beam position steady to within $20\mu m$ over a $20\,m$ lever arm. A less sophisticated version of this circuit will meet the position stability requirements for the HALL D photon source.

4.3.4 Electron beam dump

The electron beam is dumped in the horizontal plane, as shown in figure 4.4. The horizontal bend offers several advantages over dumping the beam into the ground. The tagger magnet is easier to support if it sits in the horizontal position. It is also easier to mount and service the focal plane in this position. The dump itself is also more accessible in case it needs to be serviced. An above-ground dump also affords the possibility of running parasitic beam dump experiments that do not interfere with the operation of the experimental hall.

The primary design requirement for the electron beam dump is that it have a sufficiently high capacity to handle beams of the highest intensities foreseen for HALL D. A 60KW design would provide a a healthy margin for operation of a 12 GeV beam at 3μA and sufficient capacity to handle 3μA at 20 GeV in the case of a further upgrade.

4.3.5 Beam containment and shielding

There are three factors that must be taken into account in the design of the shielding for the HALL D beam line. The first is the constraint on the background radiation level that is allowed outside the beam enclosure. The second factor is the level of radiation in the experimental hall which can generate background in the detector during normal running. The third factor is the control of hazards which may occur in the event of a failure of one or more of the beam delivery systems. The first issue has been studied by the Jefferson Laboratory Radiation Controls Group, and will be discussed further in the chapter on Civil Construction. The latter two considerations have been were studied by a working group headed by L. Keller (SLAC). A summary of their recommendations [8] follows.

Assuming that the electron beam dump is shielded to the requirements of radiation safety, the next source of background radiation in the experimental hall is the photon collimator. The most penetrating forms radiation from the collimator are muons and neutrons. A Monte Carlo simulation, assuming a 13 radiation lengths tungsten collimator followed by a sweeping magnet and 5 m of iron shielding, predicted a flux of $1.4 \times 10^3 \mu$/s incident on the detector at full operating beam intensity. This is a negligible rate compared with the trigger rate from photon interactions in the target. The flux of neutrons from the collimator is more difficult to calculate, but some fraction of 1m of concrete shielding will be needed surrounding the collimator enclosure to shield the hall from energetic neutrons.

With regard to hazards associated with the accidental failure of beam line elements or controls, the following measures were recommended in the Keller study [8] and have been incorporated into the HALL D design. The dipole string that bends the electron beam up towards the surface from the below ground and then bends it back horizontal should be connected in series so that failure of a magnet supply or current control electronics cannot result in a beam being steered into the ceiling of the tagger building. The power supply feeding this string of magnets will be protected by a meter relay that shuts off if the current varies from its desired value outside a predefined tolerance. A similar meter relay will also be used on the power supply of the tagger magnet. An electron beam collimator with a burn-through monitor will be located just upstream of the radiator to prevent a mis-steered beam from using radiator support structures as a bremsstrahlung target. Permanent magnets will be located in the upstream region of the photon beam line to bend an errant electron beam into the ground in the case that beam is present while the tagger magnet is off. An emergency beam stop will be installed in the bottom of the photon beam

line to catch the errant beam deflected by the permanent magnets. It will be equipped with a current monitor to shut down the primary beam any time electrons are sensed in the photon beam line. Ion chambers located upstream of the photon collimator, and also at the entrance to the photon beam dump behind the experiment, will monitor the total flux in the photon beam and shut off the beam if the flux exceeds a safe value.

4.4 Tagging Spectrometer

4.4.1 Specifications

To satisfy the needs of the HALL D physics program, the tagged photon spectrometer should meet the following specifications:

1. Photon energy detection from 70% to 75% of E_0 with energy resolution of about 0.1% (percentages refer to the primary beam energy E_0, i.e. "0.1%" means 12 MeV energy resolution for a 12 GeV beam.)

2. A detector system which allows a counting rate of at least 5×10^6 electrons per second per 0.1% over this range of photon energies.

3. An additional capability for photon energy detection from 25% to 90% of E_0, with less stringent resolution and count rate requirements .

4. A quadrupole magnet between the radiator and dipole spectrometer which images the beam spot on the radiator onto a line on the focal plane. This feature makes it possible to envision the use of focal plane counters with two-dimensional readout, with which one could enhance the tagging efficiency and linear polarization of the source. Focal plane detectors with two-dimensional readout are considered as a possible upgrade beyond the the baseline design presented in this chapter. Any improvements obtained using this technique would be over and above the performance figures presented in this report.

The system described below meets all of these criteria.

4.4.2 Magnet

The tagger magnet (Fig. 4.16) is an Elbek-type spectrometer similar to the existing tagger magnet in Hall B of Jefferson Lab.[10] The higher energy of the HALL D beam is largely compensated for by going to smaller bend angles,

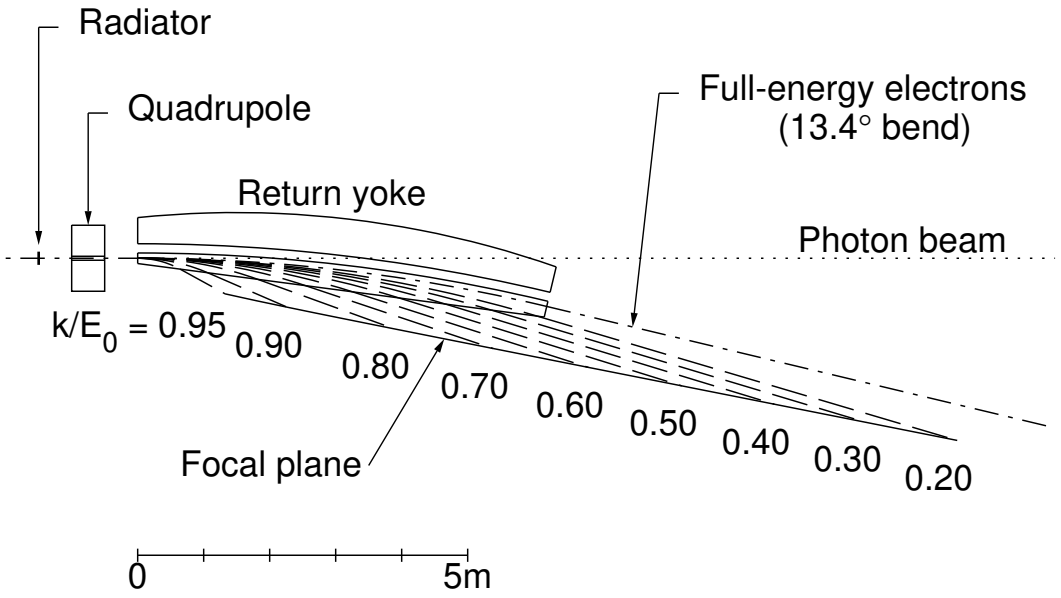

Figure 4.16: A plan view of the tagging spectrometer from above, showing the path of the primary beam and the trajectory of post-bremsstrahlung electrons of various recoil momenta.

Radius of curvature	26.7 m
Full-energy deflection	13.4^{o}
Field at 12 GeV	1.5 Tesla
Gap width	2.0 cm
Length of pole	6.1 m
Weight	100 tons
Length of focal plane (25% to 90% of E_0)	8.7 m
Coil power	800 A at 22 V

Table 4.4: Design parameters for the tagging spectrometer dipole magnet

so the sizes of the magnets are comparable, and much of the experience from Hall B can be carried over. Unlike the Hall B tagger, which bends vertically, the HALL D tagger will deflect electrons in the horizontal plane, with both the detector hall and the beam dump constructed above ground.

The parameters of the magnet are given in Table 4.4. The magnet poles themselves will form part of the vacuum system, and will be welded to a stainless steel vacuum chamber which terminates in a thin window along the length of the focal plane.

The detector package is divided into two parts: a set of 128 fixed scintillation counters spanning the full energy range from 25% to 92%, and a movable "microscope" of 64 narrow counters that is optimized for normal operation spanning the energy range from 70% to 75%.

The fixed array provides access to the full tagged photon spectrum, albeit at a modest energy resolution of 0.5% and reduced photon spectral intensity. These detectors are well suited for running with a broadband incoherent bremsstrahlung source. They enable experiments to be performed with the highest photon energies possible with the source. When running with a coherent source they play an essential role in the crystal alignment procedure, and provide a continuous monitor of the performance of the source. The microscope is needed in order to run the source in coherent mode at the highest polarization and intensities, and whenever energy resolution better than 0.5% is required. Using the microscope, the source is capable of producing photon spectral intensities in excess of 2×10^8 photons/GeV, although accidental tagging rates will limit normal operation to somewhat less than this.

Table 4.5: Geometrical parameters of the tagging spectrometer for $E_0 = 12\ GeV$: Bend = deflection angle; Drift = distance from exit edge to focal plane; Angle = angle between electron path and focal plane; cm/%E_0 = dispersion in units of cm per percent of the incident energy

k (GeV)	Bend (deg)	Drift (m)	Angle (deg)	cm/%E_0 perp.to ray	cm/%E_0 along FP
6	17.270	3.7790	6.035	1.467	13.956
7	17.664	3.2039	6.428	1.568	14.008
8	18.28	2.6276	6.992	1.716	14.096
9	19.108	2.0485	7.872	1.954	14.264
10	20.695	1.4626	9.459	2.407	14.644
11	24.608	0.8560	13.372	3.668	15.860

4.4.3 Spectrometer optics

Table 4.5 and Table 4.6 give some of the beam optics parameters as functions of the photon energy. The energy resolution and transverse position resolution were calculated using the following assumptions for the beam at the radiator:

$$\Delta E/E_0 = 0.080\% \text{ r.m.s.}$$
$$\Delta x = 1.7\, mm \text{ r.m.s.}$$
$$\Delta y = 0.5\, mm \text{ r.m.s.}$$
$$\Delta x' = .020 \text{ mr r.m.s.}$$
$$\Delta y' = .005 \text{ mr r.m.s.}$$

The intrinsic energy resolution (i.e. the energy resolution independent of detector size) is limited in most cases by the 0.08% energy spread of the primary electron beam.

At the focal plane, the characteristic bremsstrahlung angle corresponds to a few millimeters of transverse displacement. The vertical beam spot size at the radiator (0.5 mm r.m.s.) contributes a comparable amount because of the large transverse magnification in the dipole transport matrix. However, placing a quadrupole magnet between the radiator and the tagger dipole magnet reduces this magnification nearly to zero over a substantial range of photon energies, without substantially changing the other optical properties. Including the quadrupole in the design makes possible a future upgrade of the photon source by employing tagging detectors with two-dimensional readout.

Table 4.6: Optical properties and resolutions of the tagging spectrometer at the focal plane, for $E_0 = 12\ GeV$: (x x),(y y),(y y') = first-order transport matrix elements where x and y are radial and transverse coordinates respectively; the focal plane is defined by (x x')=0.; Δk_{beam} = r.m.s. energy resolution due to beam energy uncertainty; Δk_{spot} = r.m.s. energy resolution due to spot size on radiator; Δk_{tot} = total r.m.s. energy resolution excluding detector size; Δy_{tot} = transverse r.m.s. position resolution due to spot size on radiator; y_{char} = transverse size corresponding to one characteristic electron angle $\theta_{Ce} = (m/E_0)(k/(E_0 - k))$.

k	(x x)	(y y)	(y y')	Δk_{beam}	Δk_{spot}	Δk_{tot}	Δy_{tot}	y_{char}
(GeV)	(mm/mm)	(mm/mm)	(mm/mr)	($\%E_0$)	($\%E_0$)	($\%E_0$)	(mm)	(mm)
Without quadrupole:								
6	-0.701	2.737	18.882	0.080	0.081	0.114	1.372	0.804
7	-0.667	2.708	16.538	0.080	0.072	0.108	1.357	0.986
8	-0.625	2.670	14.178	0.080	0.062	0.101	1.337	1.207
9	-0.569	2.617	11.788	0.080	0.050	0.094	1.310	1.506
10	-0.494	2.539	9.341	0.080	0.035	0.087	1.270	1.989
11	-0.389	2.402	6.745	0.080	0.018	0.082	1.201	3.159
With quadrupole: (length = 50 cm, gradient = -0.4 kGauss/cm)								
6	-0.628	0.451	17.622	0.080	0.073	0.108	0.242	0.750
7	-0.583	0.348	15.121	0.080	0.063	0.102	0.190	0.901
8	-0.526	0.202	12.535	0.080	0.052	0.095	0.119	1.068
9	-0.449	-0.024	9.792	0.080	0.039	0.089	0.050	1.251
10	-0.338	-0.427	6.699	0.080	0.024	0.083	0.216	1.426
11	-0.162	-0.416	2.474	0.080	0.008	0.080	0.708	1.159

4.4.4 Tagger detectors

Focal plane microscope detectors

Since the intrinsic energy resolution along the focal plane is approximately 0.1% (Table 4.6), a detector width which spans an energy range of 0.2% could be used without seriously affecting experimental resolution (the r.m.s. deviation of a flat distribution of width W is $W/\sqrt{12} = 0.29W$. The principal limitation on detector size is imposed by the design goal of tagging collimated photons at rates up to 100 MHz over the coherent peak. The nominal collimated coherent peak has its highest intensity between about 8.5 and 9 GeV (see Fig. 4.6). However, the the tagger sees both collimated and uncollimated photons, and the total tagging rate in this region is about twice the collimated rate (see Fig. 4.6), so the actual tagging rate must be about 200 MHz. If a single phototube can count reliably at 5 MHz, then the energy range detected by a single scintillation counter should be 5 MHz / 200 MHz * 600 $MeV = 15$ $MeV = 0.12\%$ of E_0. Thus a detector width of 0.1% would satisfy the requirements of both resolution and rate. According to Table 4.5, such a detector would have a width of 3 mm perpendicular to the electron direction, and detectors for individual channels would be spaced about 30 mm apart along the focal plane.

Fixed focal plane array

Tagging of photons over the full range from 25% to 90% of E_0 is not required as part of the physics program here proposed for HALL D, but is desirable for two separate reasons. First, it will increase the flexibility of the source by allowing other possible experiments using highly polarized photons below 8 GeV, or incoherent bremsstrahlung up to 11 GeV. This capability is not available elsewhere at JLab, since the Hall B tagger will not handle beam energies above 6 GeV, and its photon polarization will be quite low for photon energies above about 4.5 GeV. Second, the process of aligning the crystal radiator for coherent bremsstrahlung requires rotation about several axes and rapid observation of the resulting energy spectra, as described in section 4.2.6. The low-energy portion of the spectrum, between about 25% and 50% of E_0, is most sensitive to these rotations, and experience with the coherent bremsstrahlung beam at Mainz [11]-[12] indicates that the alignment process would be severely compromised if photon energies below 0.5 E_0 were not measurable.

A high energy resolution in the tagger is not deemed necessary for these purposes. A counter width spanning 0.5% of E_0 is considered sufficient in most cases. For operations with an amorphous radiator, these counters would

be capable of running a broad-band photon beam with the highest intensities compatible with tagging. Crystal alignment procedures are not normally carried out at full source intensity, so rate capacity is not a limitation in that application. If a need arose to operate the source in collimated-coherent mode at lower photon energies, for example to obtain increased polarization, then full-intensity operation would always be possible by repositioning the microscope on the focal plane. In this case, the fixed array would provide be useful in fixing the energy calibration of the moveable segment. When used as the primary tagging detectors, the fixed array would be capable of pre-collimated intensities up to 80 MHz/GeV.

4.4.5 Beam dump optics

Although the full-energy beam leaving the tagger magnet is diverging in both directions, the range of angles is small enough that the beam does not blow up rapidly. For a dump distance of 30 m the r.m.s. beam size is 6.3 mmhorizontal (dominated by the 0.08% beam energy spread) and 0.7 mm vertical (combination of vertical spot size and multiple scattering in a 10^{-4} radiation length radiator.) These values scale approximately linearly with distance from the magnet to the dump, and are not very sensitive either to the quadrupole or to small rotations of the exit edge of the tagger magnet. Thus the beam dump design is quite insensitive to the beam optics, and depends only on the lateral and longitudinal spread of the shower.

4.5 Polarimetry Instrumentation

The major part of produced photons will be cut out in the proposed collimator system. In case that the radiator and collimator system are well aligned, the expected photon spectrum behind the collimators is dominated by the coherent peak. The beam parameters can be determined by using the intensity spectra of the tagging channels.

Nevertheless, in order to monitor the polarization parameters – grade (P_γ) and direction (ϵ_γ) – of the collimated photon beam it is crucial to have an independent method, either a photon polarimeter detecting the asymmetry of a process that is well understood within theory (QED), or a well known hadronic process so that the measured beam asymmetry can be compared with theoretical (or experimental) expectations. At photon energies above 5 GeV, the forward production of vector mesons is described by VMD, thus resulting in a $sin^2\theta_{hel}cos(2\psi)$ dependence of the vector meson's decay distribution where

θ_{hel}, ϕ_{hel} are the polar and azimuthal decay angles in the helicity frame and $\psi = \phi_{hel} - \epsilon_\gamma$. Acceptance studies have to be performed in order to estimate the time needed to collect sufficient statistics for these processes.

The other method, measuring the photon polarization by means of a polarimeter, can be realized by a pair polarimeter or a triplet polarimeter. It involves additional hardware components on the beamline between the collimator system and the spectrometer magnet. Both types of polarimeter require a thin radiator and a detector in a field free area followed by a dipole magnet and counters for trigger purpose.

QED based calculations for the latter process show that the angle and energy of the soft (triplet) electron is almost independent of the energy of the incident photon ($\bar{E}_{triplet} \approx 0.7 - 0.9$ MeV). The rate of this process being rather low and the technical challenge for a counter device measuring accurately the angular distribution of low energy electrons do not favor this type of polarimeter.

For pair production, on the other hand, the opening angle between the produced electron and positron decreases with increasing energy making the measurement more complicated at higher energies. A magnetic separation is not desirable because the deflection cannot been determined very accurately. The proposed polarimeter consists of a thin scintillator (d=50μm) as active target, 1.5 m in front of a silicon microstrip detector arrangement, followed by a dipole magnet and two scintillators 10 cm apart from the beamline for triggering on symmetric e^+e^- pairs. The microstrip detector consists of four layers à 512 channels silicon wavers with a spatial width for a single channel of 25 μm. The second and third layer are oriented at $\pm 60^\circ$ with respect to the first layer, the fourth perpendicular to one of the previous layers, thus allowing to measure the full angular range of produced e^+e^--pairs without any gap in the acceptance. A Monte Carlo simulation of this device including multiple scattering in the target, the microstrip detector, and foils in the vacuum system (using GEANT) shows that an analyzing power of 25 % is achievable (cf. fig 4.17). QED calculations predict an angular distribution for pair production proportional to $(1 + P_\gamma \alpha \cos 2(\phi - \epsilon_\gamma))$ with an analyzing power of $\alpha = 0.28$ for incident photons in the range of 6-10 GeV. Because of the thickness of the microstrip layers (à 300μm) it is convenient to measure the beam polarization for fifteen minutes every time when the orientation of the crystal radiator or the electron beam parameters have changed. The scintillator target as well as the detector device have to be mounted on motor driven stages so that they can be removed from the beamline.

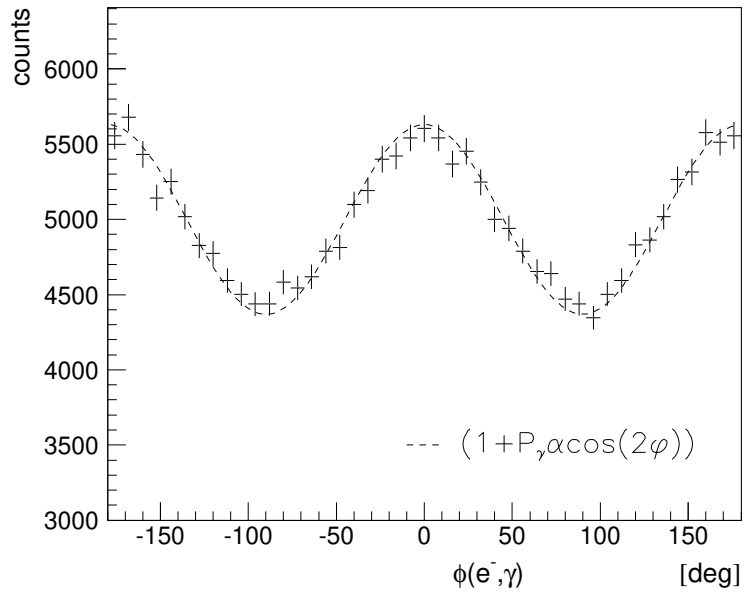

Figure 4.17: Angular distribution for pair production by linearly polarized photons as measured by a polarimeter in comparison with theoretical prediction (it dashed line). The count rate corresponds to 15 min data taking.

4.6 Operating Beam Intensity

Table 4.7 brings together the diverse set of parameters that must be considered in evaluating the optimum beam intensity at which an experiment using the coherent bremsstrahlung beam should operate. All four columns of numbers were obtained for the same beam conditions, except that the crystal orientation was adjusted to align the coherent intensity peak at the energy listed in row one. The second row labeled N_γ gives the integrated rate of beam photons in the coherent peak downstream of the collimator. Note the sharp decrease in the intensity of the coherent peak as the energy approaches the end point. By contrast, the incoherent bremsstrahlung flux is approximately constant over this range of energies. The third and fourth row show the height and width of the peak in the polarization spectrum of the beam. Rows five and six report the height and width of the peak in the tagging efficiency spectrum. The tagging efficiency is defined as the number of beam photons of a particular energy reaching the target divided by the corresponding rate in the tagging

E of peak	8 GeV	9 GeV	10 GeV	11 GeV
N_γ in peak	185 M/s	100 M/s	45 M/s	15 M/s
peak polarization	0.54	0.41	0.27	0.11
(f.w.h.m.)	(1140 MeV)	(900 MeV)	(600 MeV)	(240 MeV)
peak tagging efficiency	0.55	0.50	0.45	0.29
(f.w.h.m.)	(720 MeV)	(600 MeV)	(420 MeV)	(300 MeV)
power on collimator	5.3 W	4.7 W	4.2 W	3.8 W
power on target	810 mW	690 mW	600 mW	540 mW
total hadronic rate	385 K/s	365 K/s	350 K/s	345 K/s
tagged hadronic rate	26 K/s	14 K/s	6.3 K/s	2.1 K/s

Table 4.7: Operating parameters for an experiment using the coherent bremsstrahlung beam. The calculation assumes a 12 GeV electron beam energy and a 3.4 mm collimator 80 m downstream from a radiator of thickness 10^{-4} radiation lengths. The electron beam current is taken to be 3μA. The rates in the detector (last two rows) are calculated for a 30 cm hydrogen target and an open hadronic trigger.

focal plane. Large tagging efficiencies are required in order to make effective use of tagging. The width of the peak in the tagging efficiency spectrum determines the width of the focal plane that would be active when running with collimation. The peak integral reported in row two is summed within the f.w.h.m. tagging efficiency window. Rows seven and eight give the photon beam power that is incident on the experimental target (and photon beam dump) and the photon collimator, respectively.

The last two rows in Table 4.7 give the inclusive and tagged rates for hadronic triggers from a 30 cm liquid hydrogen target placed in the beam following the collimator. Note that the total hadronic rate is dominated by background (*i.e.* non-tagged) events associated with the low-energy component of the beam. This is why the total trigger rate is essentially constant while the flux in the coherent peak varies with peak energy over an order of magnitude. This table illustrates the value of having an electron beam energy well above the photon energy needed for the experiment.

List of Figures

4.1 Generic diagrams for hard photon production. 3
4.2 Photon energy spectrum from the Compton back-scatter source 5
4.3 Photon power spectrum from an oriented diamond radiator. . 8
4.4 Schematic plan view of the photon beam line 10
4.5 Coherent bremsstrahlung spectrum 13
4.6 Coherent bremsstrahlung spectrum after collimation. 15
4.7 Linear polarization in the coherent bremsstrahlung peak *vs* E_0 18
4.8 Linear polarization of the coherent bremsstrahlung beam *vs* E_peak 19
4.9 Maximum polarization *vs* radiator-collimator distance. . . . 21
4.10 Collimated coherent bremsstrahlung spectrum 25
4.11 Schematic illustration of crystal mounted in goniometer 27
4.12 Temperature profile of crystal at full current 31
4.13 Coherent photon spectrum for three different values of the electron beam transverse emittance. 37
4.14 Horizontal and vertical beta functions for electron beam . . . 38
4.15 Horizontal and vertical envelopes for the electron beam 39
4.16 Plan view of tagging spectrometer 43
4.17 Angular distribution for pair production by polarized photons 50

List of Tables

4.1 Figure of merit of various materials that might be used as a coherent bremsstrahlung radiator. 22
4.2 Requirements for goniometer axes 26
4.3 Assumed and projected electron beam properties 33
4.4 Tagging spectrometer parameters 44
4.5 Geometrical parameters of the tagging spectrometer for $E_0 = 12\ GeV$: Bend = deflection angle; Drift = distance from exit edge to focal plane; Angle = angle between electron path and focal plane; cm/%E_0 = dispersion in units of cm per percent of the incident energy 45
4.6 Optical properties and resolutions of the tagging spectrometer at the focal plane, for $E_0 = 12\ GeV$: (x x),(y y),(y y') = first-order transport matrix elements where x and y are radial and transverse coordinates respectively; the focal plane is defined by (x x')=0.; Δk_{beam} = r.m.s. energy resolution due to beam energy uncertainty; Δk_{spot} = r.m.s. energy resolution due to spot size on radiator; Δk_{tot} = total r.m.s. energy resolution excluding detector size; Δy_{tot} = transverse r.m.s. position resolution due to spot size on radiator; y_{char} = transverse size corresponding to one characteristic electron angle $\theta_{Ce} = (m/E_0)(k/(E_0 - k))$. 46
4.7 Operating parameters for an experiment using the coherent bremsstrahlung beam. 51

Bibliography

[1] C. Keppel. "Development of a Compton-backscattered photon source for Hall B at Jefferson Lab," *Physics with 8+ GeV Photons Workshop*, Bloomington IN, July 14-16 1997, proceedings available from Jefferson lab.

[2] W. Kaune, G. Miller, W. Oliver, R.W. Williams, and K.K. Young, *Phys. Rev. D* **11** no. 3 (1975) 478.

[3] H. Bilokon, G. Bologna, F. Celani, B. D'Ettorre Piazzoli, R. Falcioni, G. Mannocchi, and P. Picchi, *Nuclear Inst. and Meth.* **204** (1983) 299.

[4] G. Diambrini-Palazzi, *Revs. Mod. Phys.* **40** (1968) 611.

[5] U. Timm, *Fortschr. Phys.* **17** (1969) 765.

[6] J. Kellie, University of Glasgow, UK (*private communication*).

[7] J. Benesch, "Hall D Preliminary Optics Design," JLab TN 00-011 (2000) 1.

[8] L. Keller, E.S. Smith and E. Wollin, "Hall D Beam Containment Proposal," Hall D Technical Note 33 (2000) 1.

[9] S.K. Matthews *et al.*, *Nucl. Instr. and Meth.* **A 421** (1999) 23.

[10] D.I. Sober *et al.*, *Nuclear Inst. and Meth.* **A 440** (2000) 263.

[11] Anthony *et al.*, *Nucl. Instr. and Meth.* **A 301** (1991) 230.

[12] J. Hall *et al.*, *Nucl. Instr. and Meth.* **A 368** (1996) 689.